Passive and Semi-active Vibration Control of Piezoelectric Laminates

A thesis presented
by

Sam Behrens

B.E. (Mech.)

Supervisor: Dr. S. O. Reza Moheimani

The Department of Electrical and Computer Engineering
University of Newcastle, Australia

A THESIS FOR THE DEGREE OF MASTER OF ENGINEERING (RESEARCH)

December 2000

Declaration

I hereby certify that the work embodied in this thesis is the result of original research and has not been submitted for a higher degree to any other University or Institution.

Sam Behrens

December 2000

Acknowledgments

The author would like to thank Dr. S. O. Reza Moheimani from the University of Newcastle for all the guidance and help that he has provided during the past one and a half years. He has always been very patient and has made himself available for discussion and advice. I would also like to thank Reza and the Department for giving me the opportunity to develop my research skills.

I wish to extend my appreciation to Dr. Will Heath who attempted to answer all theoretical questions. The author wishes to acknowledge the help of Mr. Andrew Fleming and Mr. Matthew Smith for their assistance in this work. Also, Mr. Tim Wylie and Mr. Russel Hicks are acknowledged for their practical ideas.

On a personal note, I would like to thank my parents who offered their love and support in time of need. Also, my good friends Andrew, Marco, Scott and Eggy.

Contributions

Some of the work presented in this thesis was in collaboration with Dr. S. O. Reza Moheimani and Mr. Andrew Fleming. Dr. S. O. Reza Moheimani introduced the concept of optimal shunting damping. Design, construction and testing of the synthetic impedance circuit were in collaboration with Mr. Andrew Fleming. The negative capacitance (semi-active) controller was also in collaboration with Mr. Andrew Fleming. All other theoretical work and implementation presented was solely mine.

The simply supported beam experimental apparatus was designed by myself. Mr. Russel Hicks constructed the experimental apparatus; this work included gluing the piezoelectric laminate patches onto the beam structure and the construction of the bench clamps.

This project was considerably aided with the financial assistance of the Center of Integrated Dynamics and Control (CIDAC), Australian Research Council (ARC), University of Newcastle Postgraduate Research Scholarship (UNRS) and the Department of Electrical & Computer Engineering, University of Newcastle, Australia.

Publications

During the course of this research, a number of papers have been submitted to international journals and conferences. The following is a list of those articles, which have already appeared in an international journal or have been submitted for publication. Conference papers, which have been presented or submitted for presentation, are also listed. Technical reports and patents follow these international publications.

- **Journal Publications**

1. A. J. Fleming, S. Behrens and S. O. R. Moheimani. Synthetic impedance for implementation of piezoelectric shunt damping circuits, **36**(18):1525-6, *IEE Electronics Letters*, 31st August 2000.

2. A. J. Fleming, S. Behrens and S. O. R. Moheimani. Optimization and implementation of multi-mode piezoelectric shunt damping systems. Submitted to *IEEE/ASME Transactions on Mechatronics*, 2000.

3. S. Behrens, A. J. Fleming and S. O. R. Moheimani. Negative capacitor for multiple mode semi-active shunt damping of a piezoelectric laminate beam. Submitted to *IEE Electronics Letters*.

- **Conference Proceedings**

1. A. J. Fleming, S. Behrens and S. O. R. Moheimani. A new approach to piezoelectric shunt damping. *In: Proceedings of International Symposium on Smart Structures and Microsystems*, Hong Kong, October 2000.

2. A. J. Fleming, S. Behrens and S. O. R. Moheimani. Innovations in Piezoelectric Shunt Damping. *In: Proceedings of SPIE: Smart Structures and Devices 2000*, Melbourne Australia, 13-15th December 2000.

3. S. Behrens and S. O. R. Moheimani. Optimal resistive elements for multiple shunt damping of a piezoelectric laminate beam. *In: Proceedings of IEEE Conference on Decision and Control*, Sydney, Australia, December 2000.

- **Technical Reports**

1. A. J. Fleming, S. Behrens and S. O. R. Moheimani. Synthetic impedance for damping of smart structures. Technical Report EE0016. The Department of Electrical and Computer Engineering, University of Newcastle. March 2000.

2. S. Behrens and S. O. R. Moheimani. Optimal resistive elements for multiple mode shunt damping of a piezoelectric laminate beam. Technical Report EE0015. The Department of Electrical and Computer Engineering, University of Newcastle. March 2000.

3. S. Behrens and A. J. Fleming. Negative capacitor for multiple mode semi-active shunt damping of a piezoelectric laminate beam. Technical Report EE0045. The Department of Electrical and Computer Engineering, University of Newcastle. October 2000.

- **Patents**

An impedance synthesising arrangement, an improved vibrational damping apparatus and a method for deriving a digital signal processing algorithm. (Lodged: May 2000 - Pending)

Abstract

This thesis considers a number of related problems in the areas of passive and semi-active vibration control of piezoelectric laminates.

The thesis consists of three main parts. The first part of the thesis develops a mathematical model of a physical resonant system–piezoelectric laminated simply supported beam. It is essential to have a good understanding of the physical system so that the associated problems with passive and semi-active shunt damping can be addressed.

The second part of the thesis is concerned with problems related with current passive shunt damping techniques using a single piezoelectric laminate. One of the current problems with multiple mode techniques is determining the correct resistive damping for each resonant mode. Therefore, a systematic method is presented for determining the optimal resistance elements by minimizing the $\mathcal{H}_2$ norm of the damped system. After the design process, shunt circuits are normally implemented using discrete resistors, capacitors and virtual inductors (Riordan Gyrators). The difficulty in constructing the shunt circuits and achieving reasonable performance has been an ongoing problem. A new approach to implementing piezoelectric shunt circuits is presented. A "synthetic impedance", consisting of a voltage controlled current source and digital signal processor (DSP) system, is used to synthesize the terminal impedance of a required shunt network.

The third part of the thesis is concerned with is semi-active vibration control of piezoelectric laminates. This part addresses a number of associated problems with the current passive shunt damping schemes. The foremost being the complexity of the shunt circuits required to dampen multiple modes. They generally act to minimize structural vibration at a specific frequency - which are rarely stationary. Therefore, a new broadband semi-active shunt technique for controlling multiple modes has been developed. The "negative capacitor" controller is proposed theoretically, and then validated experimentally. The negative capacitor is similar in nature to a passive shunt damper as it uses a single piezoelectric transducer to dampen multiple modes of a flexible structure.

Contents

List of Figures

List of Tables

Chapter 1

Introduction

1.1 Piezoelectric Devices

Piezoelectric devices have shown promising applications in active, semi-active and passive vibration control [25]. Piezoelectric materials convert mechanical strains into electrical energy and vice versa. This characteristic can be exploited, allowing these piezoelectric materials to be used as both sensors and actuators.

1.1.1 Piezoelectricity

Piezoelectricity was discovered by Pierre and Jacques Curie in 1880. It is the phenomenon in which certain crystalline substances develop an electric field when subjected to pressure/forces, or conversely, exhibit a mechanical deformation when subjected to an electric field. This reciprocal coupling between mechanical and electrical energy renders piezoelectric materials useful in many applications including passive, semi-active and active vibration control.

The piezoelectric effect is found only in crystals having no center of symmetry. Examples include quartz, Rochelle salt and synthetic polycrystalline ceramics; polyvinyl-flouride (PVDF) and lead-zirconate-titanate (PZT). The last two are commonly used in vibration control.

The piezoelectric effect is based on the elastic deformation of electric dipoles in a materials crystal lattice. If an external mechanical force (or strain) deforms the crystal, an electric field is created and hence a charge distribution at the crystal's surface is generated. This phenomenon is termed the direct piezoelectric effect or "sensory effect". Applying an

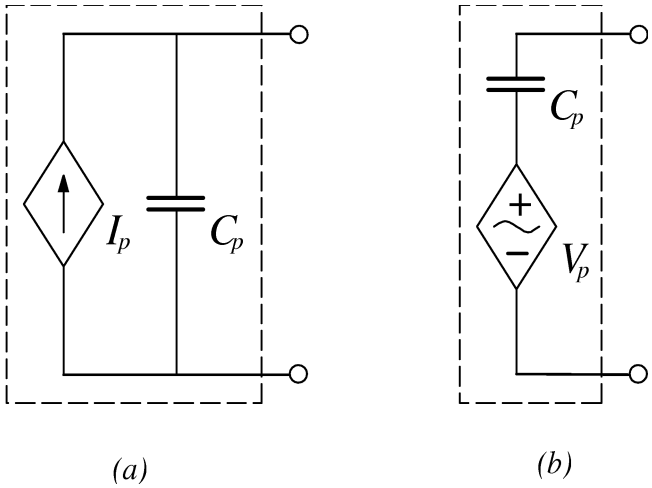

Figure 1.1: Two equivalent electrical models for a piezoelectric shunting layer: (a) parallel and (b) series piezoelectric equivalent models.

electric field causes a deformation of the dipoles, leading to a constant volume strain of the crystal. This is termed the inverse piezoelectric effect or the "actuator effect".

1.1.2 Piezoelectric Model

Piezoelectric crystals have a three-dimensional structure, i.e. crystal deformation occurs in 3 dimensions. Practical mechanical uses only require the effect in one- or two- dimensions; this can be approximated by manufacturing piezoelectric patches with large length and width to thickness ratios.

Piezoelectric transducers behave electrically like a capacitor and mechanically like a stiff spring [5]. Two equivalent electrical models for the piezoelectric shunting layer have been proposed in the literature [8, 9, 13, 26] and are presented in Figure 1.1. They are (a) parallel and (b) series piezoelectric model circuits. The quantities V_p and I_p are the equivalent voltage and current generators, which are dynamically dependent on the piezoelectric sensory effect. The most common model of the two is to model capacitor C_p in series with a dependent voltage source, as shown in Figure 1.1 (b).

1.2 Overview

Today's increasingly high speed and lightweight structures are subject to extensive vibrations that can reduce structural life and contribute to mechanical failure. Piezoelectric transducers in conjunction with appropriate circuitry, can be used as mechanical energy dissipation devices. By placing electrical impedance across the terminals of the piezoelectric element, the passive network is capable of damping structural vibrations. Researchers have used this type of suppression technique for decades.

If a simple resistor is placed across the terminals of the piezoelectric element, the piezoelectric device will act as a viscoelastic damper [13]. If the network consists of a series resistor-inductor $R-L$ circuit, the passive network combined with the inherent capacitance of the piezoelectric element creates a damped electrical resonance. The resonance can be tuned so that the piezoelectric element acts as a tuned vibrational energy absorber [13]. This damping methodology is commonly referred to as "passive shunt damping". Passive shunt damping is regarded as a simple, low cost, lightweight, and easy to implement method of controlling structural vibrations [9, 12, 14, 27, 28, 29, 30]. A desirable property of passive shunt damping is that the controlled system is guaranteed to be stable in the presence of structural uncertainties, unlike active controllers.

Flexible mechanical structures have an infinite number of resonant frequencies (or structural modes). If the tuned $R-L$ energy absorber [13] is used to minimize the vibration of a number of modes, one would need an equal number of piezoelectric element patches and shunting circuits. This is clearly impractical. Wu [28] reports a method of damping multiple vibration modes using a single piezoelectric transducer. The method differs from other multiple mode shunting schemes, see for example [9, 14]. The proposed circuit includes a "current blocker", consisting of a parallel capacitor-inductor $C-L$ network placed in series with each $R-L$ shunt circuit designed for one structural mode. Depending on the number of structural modes to be shunt damped simultaneously, a different number of $C-L$ networks are placed in series with the parallel $R-L$ shunt branch.

Although shunt damping circuits have a fixed structure, the designer is still faced with the problem of choosing component values. The blocking circuit and branch inductance values are easily found using classical circuit theory and the resonant frequencies of the structure. Currently, damping resistors are determined experimentally by observing the frequency response of the damped system and varying the resistances to achieve a desirable trade off between peak reduction and side lobe amplitude [9, 12, 14, 27, 28, 29, 30]. The

thesis proposes an optimization technique that minimizes the $\mathcal{H}_2$ norm of the damped system. This provides a systematic and reliable method for determining the resistance values of shunt damping branches.

There are also a number of implementation problems associated with single and multi-mode shunt damping techniques. Piezoelectric shunt circuits typically require large inductance values. Therefore, virtual inductors (Riordan Gyrators [22]) are required to implement the inductor elements. Virtual inductors are large in size and sensitive to component variations and non-ideal characteristics. Also, piezoelectric shunt circuits are capable of generating large voltages for moderate structural excitations. This requires that the virtual inductor circuits be constructed from high voltage operational amplifiers. At least 30 high voltage operational amplifiers are required to damp three structural modes[1]. This thesis introduces a method of implementing a specified shunt circuit with arbitrary order and complexity. The "synthetic impedance" uses a voltage dependent current source and digital signal processing (DSP) system to implement the terminal impedance of an arbitrary shunt network. It replaces physical circuits to provide effective structural damping without the problems encountered with direct circuit implementations.

Passive shunt damping generally acts to minimize structural vibration at a specific frequency [9, 12, 14, 27, 28, 29, 30]. These frequencies are rarely stationary in real applications, i.e. the resonant frequencies shift with environmental conditions. Therefore, some damping is usually added to guarantee some level of effectiveness over a range of frequencies [9, 12, 14, 27, 28, 29, 30]. Also, maximum amplitude reduction is achieved only if the shunt absorber is lightly damped and accurately tuned to the required frequency of concern. Thus, a semi-active (passive-active) vibration absorber should perform better than a purely passive shunt damper.

Many of the semi-active vibration schemes involve modifying the effective stiffness of the piezoelectric element [4, 6, 7, 20, 21]. Normally this involves switching the piezoelectric element between high (open-circuit) and low (short-circuit) stiffness states. These techniques are broadband and passive. Another type of semi-active vibration controller is the active-passive hybrid piezoelectric network (APPN), which involves using a passive shunt in conjugation with an appropriate broadband active controller (e.g. a simple $R-L$ passive shunt with a LQG active controller). This method is claimed to be more effective than a system with separated active and passive control schemes [1, 3, 23, 24].

[1] Based on a series circuit configuration with "current blockers" in every branch, as shown in reference to [28] .

A new technique for semi-active (passive-active) controlling piezoelectric laminated structures is proposed in this thesis. The effect of the "negative capacitor" is studied theoretically and then validated experimentally on a piezoelectric laminated simply supported beam. The negative capacitor is similar in nature to passive shunt damping techniques [9, 12, 14, 27, 28, 29, 30], as a single piezoelectric transducer is used together with an attached electrical impedance. While achieving comparable performance, the negative capacitor has a number of advantages over current passive shunt damping systems. It is simpler to implement and has less sensitivity to environmental variations.

1.3 Motivations and Application

Vibration control of smart structures is regarded as an active area of research in the aerospace industry. Aerospace research companies, such as Boeing, Lockheed-Martin, NASA and other US government agencies, are investing large capital to investigate novel methods for controlling structural vibration.

Listed below are examples of some interesting applications:

- Modern commercial or military aircraft, for example the Boeing-Lockheed Martin-Pratt & Whitney F-22 fighter shown in Figure 1.2, is often required to fly at high velocities and high angles of attack. In this type of operation, the highly turbulent flow from the leading edge of the wings can impinge on the vertical tails of the aircraft, causing acute buffeting vibrations. This vibration increases the fatigue of critical structural members, requiring frequent inspections, reducing the aircraft's flight time, and shortening the useful life of the aircraft.

- Novelty items, such as the prevention of vibration in snow skies. A snow ski company, K2 Sports (*http://www.k2skis.com*), has developed "Smart Ski Technology". They claim their skis provide a smooth, chatter-free ride that reduces skier fatigue and increases a skier's control. A piezoelectric patch is embedded into the ski composite structure, where the piezoelectric patch absorbs mechanical energy and dissipates this energy through a simple LED light.

Figure 1.2: F-22 Jet Fighter (Boeing-Lockheed Martin-Pratt & Whitney 2000).

Figure 1.3: "Smart Ski Technology" (K2 Sport 2000).

1.4 Outline of the Thesis

The thesis is organized as follows:

- Chapter 2: **Physical Modeling:** A mathematical model of a resonant structure, a piezoelectric laminated simply supported beam, is developed to assist with the design of different passive and semi-active vibration control strategies. The modeling techniques are based on *modal analysis* and the one dimensional Euler-Bernoulli beam equation. The model of the resonant system is modified to include the effect of approximate experimental simply supported boundary conditions.

- Chapter 3: **Piezoelectric Passive Shunt Damping:** Current passive shunt damping techniques of multiple mode configurations is examined. Modeling of the composite system, i.e. the passive shunt controller present on the damped system, is derived in state-space form. A $\mathcal{H}_2$ norm optimization technique is developed to determine the optimal multiple mode shunt resistances. A theoretical finding of optimal resistive damping elements is validated through experimental results on the simply supported beam. All experimental shunt circuits were constructed using discrete elements, e.g. resistors, simulated inductors (Riordan Gyrators) and capacitors.

- Chapter 4: **Synthetic Impedance:** Current research implementation of discrete shunt circuits raise many implementation problems, such as non-linear circuits. A new method is introduced which tackles the discrete shunt implementation problems. "Synthetic impedance" is established based on a voltage controlled current source model and a digital signal processor (DSP). The synthetic impedance is utilized to simulate two multiple mode shunt circuits, as described in Chapter 3. The synthetic impedance is compared experimentally to the direct circuit method. The theoretical damped response of the piezoelectric laminate beam is critically assessed against the experimentally proposed synthetic impedance and direct circuit methods.

- Chapter 5: **Shunt Damping using a Negative Capacitance Circuit:** A passive shunt absorber acts to minimize structural vibration at a specific frequency which is rarely stationary in real applications. Maximum amplitude reduction is only achieved if the resonant shunt absorber is lightly damped and accurately tuned. A semi-active (passive-active) vibration controller should perform better than a purely passive shunt. This chapter introduces theoretically, a new type of broadband semi-

active piezoelectric shunt controller. The "negative capacitance" controller incorporates some fundamental properties of the piezoelectric element into the control strategy. This new passive-active controller is validated on the simply supported piezoelectric laminated beam, with promising results.

- Chapter 6: **Conclusion and Future Development:** This chapter will conclude the thesis with final remarks from each chapter. Suggestion for future research are also raised.

Chapter 2

Physical Modeling

A mathematical model has been developed to assist in the development of passive and semi-active vibration shunt controllers. One of the most popular methods of modeling piezoelectric laminate structures is *modal analysis* [16]. Since we are interested in modeling a piezoelectric laminated simply supported beam, the governing equation is the modified Euler-Bernoulli beam equation. A model of experimental boundary conditions has also been developed, in which shim material replaces the *ideal* pinned boundary conditions.

Consider the piezoelectric laminate simply supported beam in Figure 2.1. A pair of piezoelectric patches is bonded to the resonant structure surface. One piezoelectric layer will be used as an actuator and the other for shunting. The subscripts "a", "b" and "s" correspond to the actuating piezoelectric layer, the beam and the shunting piezoelectric layer respectively.

Using the modal analysis procedure, the position function $y(x,t)$ is expanded as an infinite series in the form:

$$y(x,t) = \sum_{i=1}^{\infty} q_i(t)\phi_i(x), \tag{2.1}$$

where $q_i(t)$ is referred to as the *modal displacement* or *generalized coordinate* and $\phi_i(x)$ are the eigenfunctions satisfying the ordinary differential equations (ODEs). Before considering this approach we need to consider the piezoelectric actuator and shunting sensor dynamics.

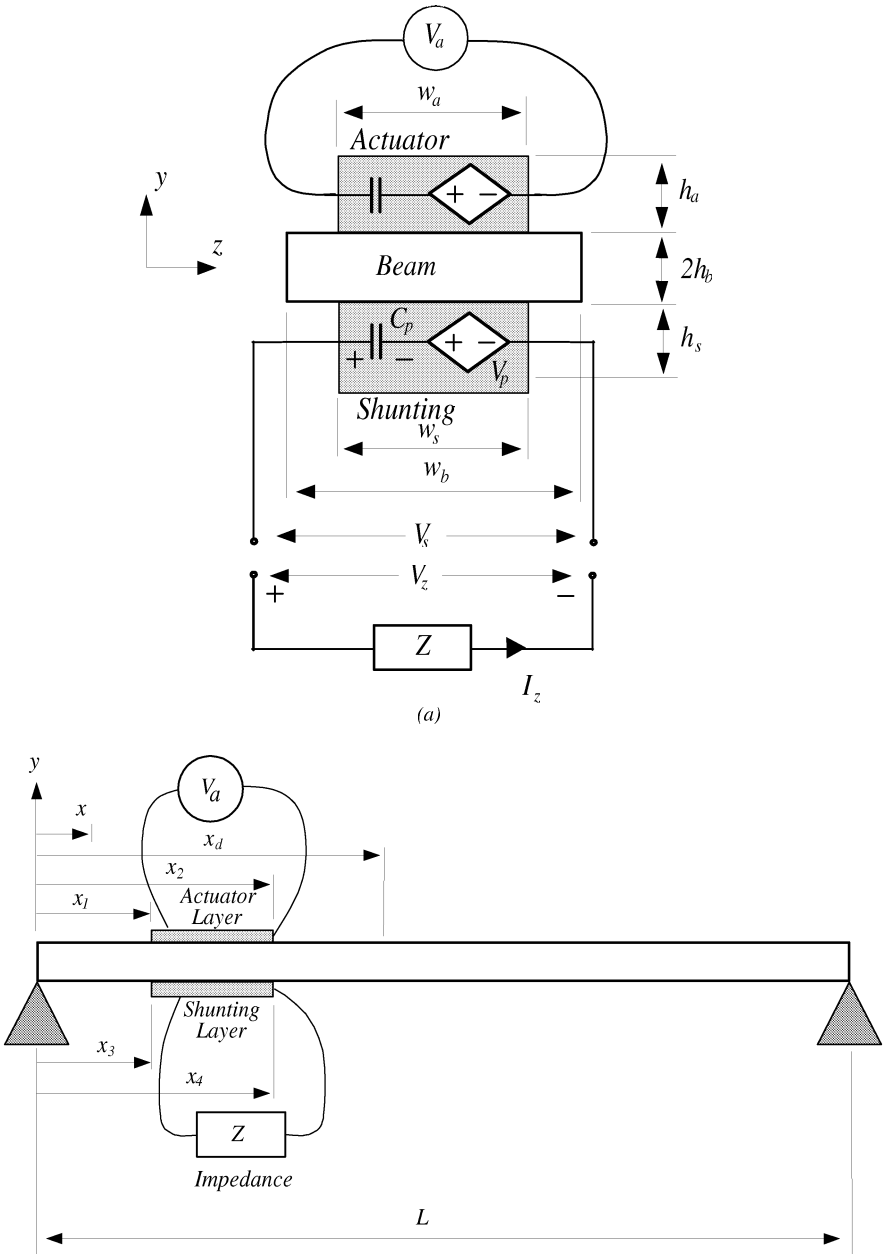

Figure 2.1: (a) Cross-section of the beam with piezoelectric laminates present; and (b) the piezoelectric laminated simply supported beam.

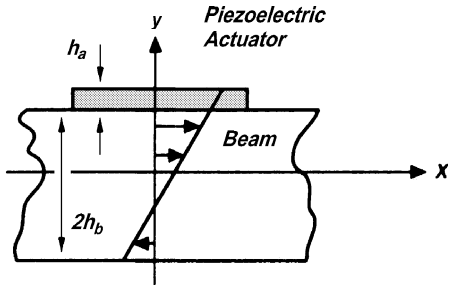

Figure 2.2: Anti-symmetric piezoelectric actuator.

2.1 Dynamics of the Beam with a Piezoelectric Actuator

A common arrangement for the piezoelectric actuator is the one dimensional anti-symmetric *wafer* configuration [10], shown in Figure 2.2. The actuator is bonded to the surface of the resonant structure using a strong adhesive material. This configuration assumes that the piezoelectric element is very long in the x direction compared to the z direction, i.e. $l_a = (x_2 - x_1) \gg w_a \gg h_a$ (refer to Figures 2.1 and 2.2). Since the patch is longer in the x direction, compared to the y and z directions, when a voltage is applied across the electrodes (in the direction of polarization), the actuator induces surface strains to the beam in the x direction.

Before making any derivations we must make some important assumptions. The first assumption is that the structure (the beam) is covered by a thin layer of piezoelectric material of thickness h_a, which is perfectly adhered to the beam. We also assume that the piezoelectric element only strains in the x direction, since $l_a = (x_2 - x_1) \gg w_a \gg h_a$. And finally, if the piezoelectric patch is thin and lightweight, compared to the beam system, we can ignore the inertial effects.

When a voltage is applied across the parallel plates of an unconstrained (i.e. not attached) piezoelectric element, the actuator will strain by an amount ε_a, in the x direction as depicted by [10]

$$\varepsilon_a = \frac{d_{31} V_a(t)}{h_a}, \tag{2.2}$$

where $V_a(t)$ is the applied voltage in the direction of polarization, h_a is the actuator thick-

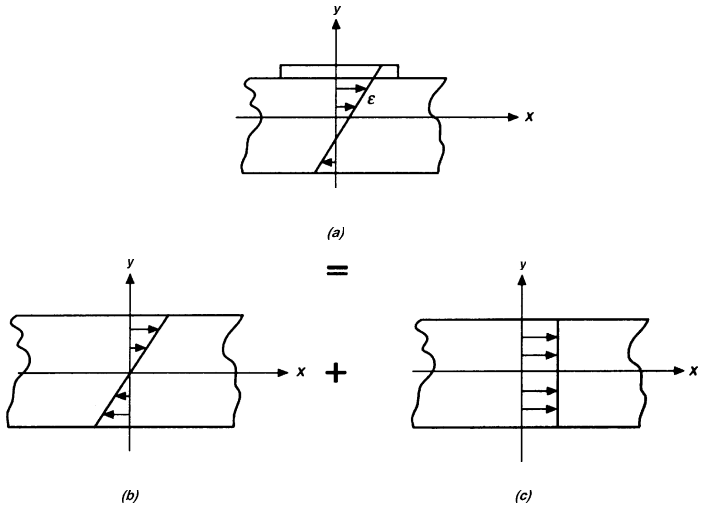

Figure 2.3: Decomposition of *wafer* strain distribution: (a) asymmetric strain distribution, (b) flexural component and (c) longitudinal component [10].

ness and d_{31} is the piezoelectric material strain constant.

When a voltage is applied across the bonded piezoelectric element, it will attempt to deform but will be constrained due to the stiffness of the beam. Due to its symmetric nature, the beam will both bend and elongate, leading to an asymmetric strain distribution, as shown in Figure 2.3. We assume that the strain distribution is linear, thus

$$\varepsilon(y) = Cy + \varepsilon_0, \tag{2.3}$$

where C is the slope and ε_0 is the uniform strain component at the y intercept.

Consider the asymmetric strain distribution show in Figure 2.3. Using Hooke's law the stress distribution within the beam structure can be expressed as

$$\sigma_b(y) = E_b(Cy + \varepsilon_0),$$

where E_b is Young's elastic modulus of the beam material. The linear stress distribution, within the piezoelectric actuator $\sigma_a(y)$, is thus

$$\sigma_a(y) = E_a(Cy + \varepsilon_0 - \varepsilon_a),$$

where E_a is Young's elastic modulus of the piezoelectric material.

By applying moment equilibrium about the centre of the beam and force equilibrium in the x direction, the following two relationships can be formulated:

$$\int_{-h_b}^{h_b} \sigma_b(y) y dy + \int_{h_b}^{h_b+h_a} \sigma_a(y) y dy = 0 \tag{2.4}$$

and

$$\int_{-h_b}^{h_b} \sigma_b(y) dy + \int_{h_b}^{h_b+h_a} \sigma_a(y) dy = 0, \tag{2.5}$$

where h_b is the half-thickness of the beam.

Integrating (2.4) and (2.5) and solving for the unknowns C and ε_0, we obtain

$$\varepsilon_0 = K^L \varepsilon_a,$$

where K^L is specified by [10]

$$K^L = \frac{E_a h_a (8E_b h_b^3 + E_a h_a^3)}{16E_b^2 h_b^4 + E_b E_a (32 h_b^3 h_a + 24 h_b^2 h_a^2 + 8 h_b h_a^3) + E_a^2 h_a^4} \tag{2.6}$$

and the slope C is given by

$$C = K^f \varepsilon_a,$$

where the material-geometric constant K^f is specified by [10]

$$K^f = \frac{E_b E_a h_b h_a (2h_b + h_a)}{16E_b^2 h_b^4 + E_b E_a (32 h_b^3 h_a + 24 h_b^2 h_a^2 + 8 h_b h_a^3) + E_a^2 h_a^4}. \tag{2.7}$$

The induced moment distribution, M_a, beneath the actuator in the beam structure is given by

$$M_a = E_b I_b K^f \varepsilon_a, \tag{2.8}$$

where the strain ε_a is related to the applied voltage via (2.2) and I_b is the moment of inertia of the beam.

2.2 Dynamics of the Beam with a Piezoelectric Shunt Sensor

We make similar assumptions for the piezoelectric shunt sensor as the actuator layer [10]. The shunt sensor is very thin, lightweight, perfectly adhered to the beam and only strains in the x direction. When the beam is strained, it results in the following strain distribution,

$$\varepsilon_s(x,t) = -\left(h_b + h_s\right)\frac{\partial^2 y(x,t)}{\partial x^2}. \tag{2.9}$$

Due to the piezoelectric effect, this strain produces a charge distribution per unit area $q(x,t)$, given by [10]

$$q(x,t) = \left(\frac{k_{31}^{'2}}{g_{31}}\right)\varepsilon_s(x,t), \tag{2.10}$$

where k_{31} is the piezoelectric electromagnetic coupling constant and g_{31} is the piezoelectric stress constant. The total charge accumulated on the shunting layer can be found by integrating $q(x,t)$ over the entire surface area of the piezoelectric element (with reference to Figure 2.1), as

$$Q(t) = \int_{x_3}^{x_4} w_s q(x,t)dx = -w_s\left(h_b + h_s\right)\left(\frac{k_{31}^{'2}}{g_{31}}\right)\frac{\partial y(x,t)}{\partial x}\bigg|_{x_3}^{x_4}. \tag{2.11}$$

Since the piezoelectric patch, once charged, can be considered as a simple parallel plate capacitor, the voltage across the two layers $v_s(t)$, can be found to be

$$v_s(t) = \frac{Q(t)}{C_{up}w_s(x_4 - x_3)} = C_s\frac{\partial y(x,t)}{\partial x}\bigg|_{x_3}^{x_4},$$

where C_{up} is the capacitance per unit area for the piezoelectric shunting layer. The above equation can be simplified to show that C_s is a geometric constant, which can be determined from (2.10) and (2.11), thus

$$C_s = \frac{-w_s}{C_p}\left(h_b + h_s\right)\left(\frac{k_{31}^2}{g_{31}}\right), \tag{2.12}$$

where C_p is the capacitance of the shunt sensor.

2.3 Dynamical Model of the Beam System

Dynamics of the beam is governed by a modified Euler-Bernoulli beam equation [10],

$$\frac{\partial^2}{\partial x^2}\left[E_b I_b \frac{\partial^2 y(x,t)}{\partial x^2} - M_a\right] + \rho A_r \frac{\partial^2 y(x,t)}{\partial t^2} = 0, \tag{2.13}$$

where E_b, I_b, A_r and ρ represent the Young's modulus, moment of inertia, cross-section area and linear mass density of the beam respectively. Furthermore, the additional term $M_a = C_a v_a(x,t)$ is the moment applied to the beam by the piezoelectric actuator layer, as shown in (2.8). The model assumes that the piezoelectric laminate is very thin compared to the thickness of the beam element and that the beam deflects in x dimension.

We use the modal analysis expression (2.1) to find the particular solution of two essential ordinary differential equations (ODEs). That is, from the unforced equation of motion

$$\frac{\partial^2}{\partial x^2}\left[E_b I_b \frac{\partial^2 y(x,t)}{\partial x^2}\right] + \rho A_r \frac{\partial^2 y(x,t)}{\partial t^2} = 0$$

after substitution of $y_i(x,t) = \phi_i(x) q_i(t)$, we have

$$\frac{\partial^4 \phi_i q_i}{\partial x^4} + \frac{\rho A_r}{E_b I_b}\frac{\partial^2 \phi_i q_i}{\partial t^2} = 0$$

which reduces to

$$\frac{1}{\phi_i}\phi_i'''' = -\frac{\rho A_r}{E_b I_b}\frac{\ddot{q}_i}{q_i}.$$

Now both expressions must be equal to a constant ω_i^2. That is,

$$\frac{1}{\phi_i}\phi_i'''' = -\frac{\rho A_r}{E_b I_b}\frac{\ddot{q}_i}{q_i} = \omega_i^2,$$

which yields two ordinary linear differential equations, namely

$$\ddot{q}_i + w_i^2 q_i = 0 \tag{2.14}$$

and

$$\phi_i'''' - \beta_i^4 \phi_i = 0 \tag{2.15}$$

where, by definition

$$\beta_i^4 \triangleq \omega_i^2 \frac{\rho A_r}{E_b I_b}.$$

We apply the simply supported boundary conditions to the two ordinary differential equations (2.14) and (2.15). At $x = 0$, the pinned boundary conditions are

$$y(0,t) = 0 \tag{2.16}$$

and

$$E_b I_b \frac{\partial y(0,t)}{\partial x} = 0 \tag{2.17}$$

and at length $x = L$, we also have

$$y(L,t) = 0 \tag{2.18}$$

and

$$E_b I_b \frac{\partial y(L,t)}{\partial x} = 0. \tag{2.19}$$

To solve the partial differential equation (2.13), the mode shapes $\phi_i(x)$ are assumed to be expressed using the eigenfunction solution,

$$\phi_i(x) = \bar{A}_i \sin \beta_i x + \bar{B}_i \cos \beta_i x + \bar{C}_i \sinh \beta_i x + \bar{D}_i \cosh \beta_i x.$$

The solution of the characteristic equation is

$$\sin(\beta_i L) = 0 \tag{2.20}$$

and to which corresponds the infinite set of eigenfunctions,

$$\beta_i L = i\pi \quad if \quad i = 1, 2, ... \ .$$

The *resonant* frequencies ω_i are related to β_i via

$$\omega_i = {\beta_i}^2 \sqrt{\frac{E_b I_b}{\rho A_r}} = \left(\frac{i\pi}{L}\right)^2 \sqrt{\frac{E_b I_b}{\rho A_r}}. \tag{2.21}$$

The mode shapes $\phi_i(x)$ are generally normalized according to the orthogonality conditions

$$\int_0^L \phi_i(x)\phi_j(x) E_b I_b \, dx = {\omega_i}^2 \delta_{ij} \tag{2.22}$$

and

$$\int_0^L \phi_i(x)\phi_j(x) \rho A_r \, dx = \delta_{ij}, \tag{2.23}$$

where the *Kronecker delta* function is defined by

$$\delta_{ij} = \begin{cases} 1 & if \quad i = j \\ 0 & if \quad i \neq j \end{cases} .$$

The mode shapes are found to be of the form

$$\phi_i(x) = \sqrt{\frac{2}{\rho A_r L}} \sin\left(\frac{i\pi x}{L}\right). \tag{2.24}$$

To formulate the dynamical response of the system, Lagrange's equation [10, 16] will be used. Lagrange's equation provides a general formulation for the equations of motion of a dynamical system. The system's kinetic energy $T(t)$ can be written as

$$T(t) = \frac{1}{2}\int_0^L \dot{y}(x,t)^2 \rho A_r \, dx,$$

in which the constant symmetric mass coefficients m_{ij} depend on the continuous system mass properties and the eigenfunctions $\phi_i(x)$. After substitution of (2.1) and using the orthogonality conditions (2.22) and (2.23) of the mode shapes, we define $T(t)$ as

$$T(t) = \frac{1}{2}\sum_{i=1}^{\infty} \varphi_i \dot{q}_i{}^2(t), \tag{2.25}$$

where we define $\varphi_i = \int_0^L \phi_i^2(x)\rho A_r \, dx$.

Similarly, the potential energy can be expressed as

$$V(t) = \frac{1}{2}\int_0^L y''(x,t)(t,x)^2 E_b I_b \, dx$$

due to the orthogonality conditions. This expression reduces to

$$V(t) = \frac{1}{2}\sum_{i=1}^{\infty} k_i q_i^2(t) = -\frac{1}{2}\sum_{i=1}^{\infty} \omega_i^2 \varphi_i q_i^2(t). \tag{2.26}$$

The stiffness coefficients $k_i = \omega_i^2 \varphi_i$ depend on the continuous system stiffness properties and derivatives of the eigenfunctions $\phi_i(x)$ [16].

External forces are generally regarded as non-conservative, so that Lagrange's equation of motion has the form

$$\frac{d}{dt}\left(\frac{\partial T}{\partial \dot{q}_k}\right) - \frac{\partial T}{\partial q_k} + \frac{\partial V}{\partial q_k} = Q_k(t) \quad if \quad k = 1, 2, \ldots, N \quad . \tag{2.27}$$

where the general non-conservative forces $Q_k(t)$ are determined to be [17],

$$Q_k(t) = \int_0^L C_a v_a''(t,x)\phi_i(x)\,dx.$$

The constant C_a is defined in the previous section as

$$C_a \triangleq \frac{E_b I_b K^f d_{31}}{h_a}$$

and the second derivative of the actuating voltage function can be determined as

$$v_a''(x,t) = \frac{\partial^2 v_a(x,t)}{\partial x^2}.$$

Now, the applied voltage to the piezoelectric actuator goes through a step change at the boundaries of the "perfectly bonded" element and hence the spatial derivative is two impulse functions of opposite sign. That is [10, 17]

$$v_a''(x,t) = [\delta'(x-x_1) - \delta'(x-x_2)]v_a(t).$$

Using the Lagrange equation of motion (2.27) and substitution of (2.25) and (2.26), we get an equation in terms of the input voltage $V_a(s)$

$$q_i(s)\rho A(s^2 + w_i^2) = C_a[\phi_i'(x_1) - \phi_i'(x_2)]V_a(s)$$

and substituting $Y_i(x,s) = \phi_i(x)q_i(s)$ we can formulate the total response:

$$\frac{Y(x,s)}{V_a(s)} = \sum_{i=1}^{\infty} \frac{C_a[\phi_i'(x_1) - \phi_i'(x_2)]\phi_i(x)}{s^2 + w_i^2}. \tag{2.28}$$

The above equation describes the elastic deflection of the entire flexible beam due to an applied voltage to the piezoelectric actuator. To find the transfer function between the actuator voltage and the shunting sensor voltage, we note that [17]

$$v_s(t) = C_s \sum_{i=1}^{\infty} q_i(t)(\phi_i'(x_3) - \phi_i'(x_4)). \tag{2.29}$$

By taking the Laplace transform of (2.29), we obtain the following expression

$$V_s(s) = C_s(\phi_i'(x_3) - \phi_i'(x_4)) \sum_{i=1}^{\infty} q_i(s) = C_s(\phi_i'(x_3) - \phi_i'(x_4)) \sum_{i=1}^{\infty} \frac{Y_i(x,s)}{\phi_i(x)}. \tag{2.30}$$

With the above expression, the transfer function from the applied actuator voltage to the shunt sensor voltage is

$$\frac{V_s(s)}{V_a(s)} = \sum_{i=1}^{\infty} \frac{C_s C_a[\phi_i'(x_1) - \phi_i'(x_2)][\phi_i'(x_3) - \phi_i'(x_4)]}{s^2 + w_i^2}. \tag{2.31}$$

Note that the (2.31) assumes no natural damping. This is somewhat unrealistic and usually damping is added ($2\zeta_i w_i s$) at some arbitrary point in the formulation of the transfer function. And thus

$$G_{yv}(x,s) \triangleq \frac{Y(x,s)}{V_a(s)} = \sum_{i=1}^{\infty} \frac{C_a[\phi_i'(x_1) - \phi_i'(x_2)]\phi_i(x)}{s^2 + 2\zeta_i w_i s + w_i^2} \tag{2.32}$$

and

$$G_{vv}(s) \triangleq \frac{V_s(s)}{V_a(s)} = \sum_{i=1}^{\infty} \frac{C_s C_a[\phi_i'(x_1) - \phi_i'(x_2)][\phi_i'(x_3) - \phi_i'(x_4)]}{s^2 + 2\zeta_i w_i s + w_i^2}. \tag{2.33}$$

The above transfer functions (2.32) and (2.33) can be simplified to a more general second order system, as

$$G_\infty(s) = \sum_{i=1}^{\infty} \frac{F_i}{s^2 + 2\zeta_i \omega_i s + \omega_i^2}, \tag{2.34}$$

where the F_i are constant with respect to frequency, position and shape of the piezoelectric actuator/shunting layers. Here, ζ_i are the damping ratios that is often determined experimentally and ω_i are the modal frequencies. In a typical control design scenario, the designer is often interested only in a particular bandwidth. Therefore, the transfer function (2.34) is simplified by truncating the out-of-bandwidth mode, i.e.

$$G_N(s) = \sum_{i=1}^{N} \frac{F_i}{s^2 + 2\zeta_i \omega_i s + \omega_i^2}. \tag{2.35}$$

A drawback of this approach is that the truncated high orders modes may contribute to low frequency dynamics in the form of distortion of the zero location. This problem is considered in Section 2.6. The state-space equation for $G_{yv}(x,s)$ and $G_{vv}(s)$ can be represented as

$$\begin{aligned} \dot{\mathbf{x}}_b &= \mathbf{A}\mathbf{x}_b + \mathbf{B}V_a \\ Y &= \mathbf{C}_Y \mathbf{x}_b \\ V_s &= \mathbf{C}_{V_s} \mathbf{x}_b, \end{aligned} \tag{2.36}$$

where $\mathbf{x}_b$ corresponds to the beam states, then $\mathbf{A}$ and $\mathbf{B}$ are as follows:

$$\mathbf{A} = \begin{bmatrix} 0 & 1 & & 0 & 0 \\ -\omega_1^2 & -2\zeta_1\omega_1 & & 0 & 0 \\ & & \ddots & & \\ 0 & 0 & & 0 & 1 \\ 0 & 0 & & -\omega_i^2 & -2\zeta_i\omega_i \end{bmatrix}$$

and

$$\mathbf{B} = \begin{bmatrix} 0 & 1 & \cdots & 0 & 1 \end{bmatrix}^T.$$

For a general case, $\mathbf{C}_Y$ and $\mathbf{C}_{V_s}$ is of the form

$$\begin{bmatrix} F_1 & 0 & \cdots & F_i & 0 \end{bmatrix},$$

where $F_1, ..., F_i$ depends on $Y(x, s)$ and $V_s(s)$.

2.4 Experimental Boundary Conditions

The pinned boundary conditions for the simply supported beam described in Section 2.3 are difficult to simulate under laboratory conditions due to their physical nature. An alternative method is needed to simulate the required experimental boundary conditions. One possible solution is to replace the pinned boundary conditions with a *weak torsional spring* [19], as in Figure 2.4.

To construct the required experimental spring boundary conditions, we attach a shim material to each end of the experimental beam, as shown in Figure 2.5. The other end of the shim material is attached to a fixed structure. The shim material acts as a fixed-moment beam [19], as shown in Figure 2.6.

If we replace the *ideal* boundary conditions with the shim material, the new boundary conditions change the system's dynamics, especially the resonant frequencies ω_i. We need to modify the Euler-Bernoulli beam equation to include the shim boundary conditions (SBC), which are [19]: (refer to page 22)

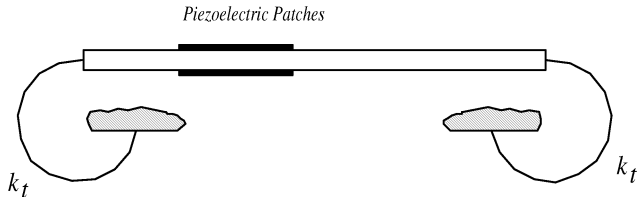

Figure 2.4: Torsional spring boundary conditions.

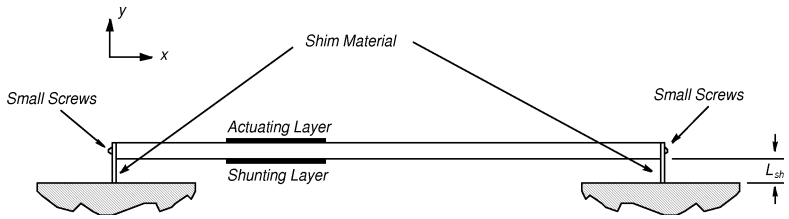

Figure 2.5: Experimental boundary conditions, $L_{sh} = 5mm$.

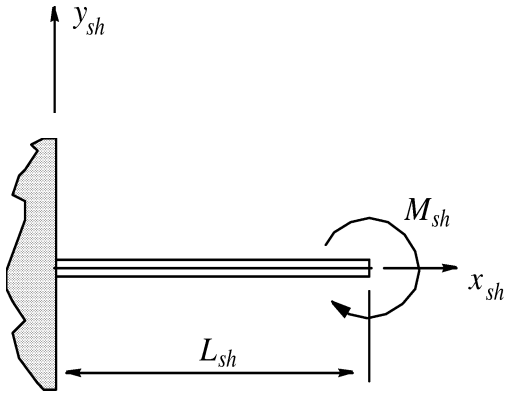

Figure 2.6: Shim material with a moment load at the free end, i.e. a fixed-moment beam.

$$\begin{aligned} y(0,t) &= y(L,t) = 0, \\ E_b I_b \frac{\partial^2 y(0,t)}{\partial x^2} &= k_t \frac{\partial y(0,t)}{\partial x} \end{aligned}$$

and

$$E_b I_b \frac{\partial^2 y(L,t)}{\partial x^2} = k_t \frac{\partial y(L,t)}{\partial x}, \tag{2.37}$$

where k_t is the torsional spring constant of the shim material. Using the above boundary conditions, the natural frequencies ω_i can be determined. Assuming a solution of the form, as in Section 2.3,

$$\phi_i(x) = \bar{A}_i \sin\beta_i x + \bar{B}_i \cos\beta_i x + \bar{C}_i \sinh\beta_i x + \bar{D}_i \cosh\beta_i x$$

and using the first three boundary conditions (2.37), replacing $\bar{A}_i$, $\bar{C}_i$ and $\bar{B}_i$, we obtain

$$\begin{aligned} \bar{A}_i &= \frac{\bar{D}_i(k_t\cos(\beta_i L) - k_t\cosh(\beta_i L) - 2\beta_i E_b I_b \sinh(\beta_i L))}{k_t(\sin(\beta_i L) - \sinh(\beta_i L))}, \\ \bar{C}_i &= \frac{\bar{D}_i(-k_t\cos(\beta_i L) + k_t\cosh(\beta_i L) + 2\beta_i E_b I_b \sinh(\beta_i L))}{k_t(\sin(\beta_i L) - \sinh(\beta_i L))} \end{aligned}$$

and

$$\bar{B}_i = -\bar{D}_i.$$

Using the last boundary condition in (2.37),

$$E_b I_b \frac{\partial^2 y(L,t)}{\partial x^2} = k_t \frac{\partial y(L,t)}{\partial x},$$

the following non-linear equation can be derived

$$\begin{aligned} 0 &= k_t^2 - k_t\cos(\beta_i L)\cosh(\beta_i L) + 2\beta_i E_b I_b k_t \cosh(\beta_i L)\sin(\beta_i L) \\ &\quad -2\beta_i E_b I_b k_t \cos(\beta_i L)\sinh(\beta_i L) + 4\beta_i^2 E_b^2 I_b^2 \sin(\beta_i L)\sinh(\beta_i L). \end{aligned} \tag{2.38}$$

Using a numerical method to determine β_i, we can determine the natural frequencies of the experimental structure by

$$\omega_i = {\beta_i}^2 \sqrt{\frac{E_b I_b}{\rho A_r}}. \tag{2.39}$$

We can assume that the mode shapes retain their original form of $\phi_i(x) = \sqrt{\frac{2}{\rho A_r L}} \sin\left(\frac{i\pi x}{L}\right)$, since only the resonant frequencies are affected by the shim boundary conditions. The experimental simply supported beam still retains its symmetric mode shapes.

To determine the experimental shim stiffness k_t, we can model the shim material as a simple beam, therefore, we are able to derive a solution using fundamental beam properties. From [15], the following relationship holds for a moment load at the end of a cantilever beam (refer to Figure 2.6),

$$y_{sh}(x_{sh}) = \frac{M_{sh} x_{sh}^2}{2E_{sh} I_{sh}} \quad if \quad 0 \leq x_{sh} \leq L_{sh}, \tag{2.40}$$

where E_{sh} is the Young's elastic modulus of the shim material and I_{sh} is the moment of inertia of the shim material. By differentiating with respect to x_{sh}, we obtain

$$\left.\frac{dy_{sh}(x_{sh})}{dx_{sh}}\right|_{x_{sh}=L_{sh}} = \left.\frac{M_{sh} x_{sh}}{E_{sh} I_{sh}}\right|_{x_{sh}=L_{sh}} = \frac{M_{sh} L_{sh}}{E_{sh} I_{sh}}. \tag{2.41}$$

Approximating the torsional spring behavior of the shim material, for small angles, the deflection will be described by

$$\theta \approx \left.\frac{dy_{sh}(x_{sh})}{dx_{sh}}\right|_{x_{sh}=L_{sh}}, \tag{2.42}$$

where θ is the angle of twist of the shim from its neutral axis. For a torsional spring, the following equation is also valid for small angles [15],

$$M_{sh} \approx k_t \theta. \tag{2.43}$$

Therefore, from (2.42) and (2.43), we obtain

$$k_t = \frac{M_{sh}}{\theta} = \frac{E_{sh} I_{sh}}{L_{sh}}. \tag{2.44}$$

Using the shim parameters shown in Table C.1, we obtain $k_t \approx 2N/m$. Therefore, the experimental boundary conditions are equivalent to the ideal boundary scenario, i.e. $E_b I_b \frac{\partial^2 y(0,t)}{\partial x^2} = E_b I_b \frac{\partial^2 y(L,t)}{\partial x^2} \approx 0$ and $y(0,t) = y(L,t) = 0$.

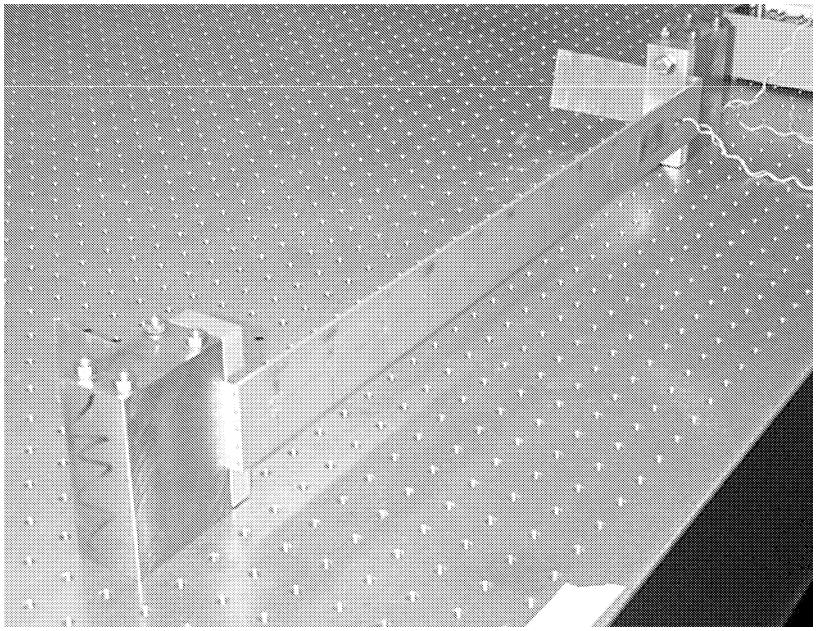

Figure 2.7: Experimental simply supported piezoelectric laminated beam, $L_{sh} = 5mm$.

2.5 Verification of Experimental Boundary Condition

The experimental beam apparatus, as illustrated in Figure 2.7, consists of a uniform aluminum beam of a rectangular cross section. The beam parameters are given in Table B.1. A pair of piezoelectric ceramic patches are attached symmetrically to either side of the beam structure at $0.05m$ from one of the shim boundary conditions, i.e. $x_1 = x_3 = 0.05m$ with reference to Figure 2.1. The piezoceramic elements used on the experimental structure are PIC151 PZT (lead-zirconate-titanate) patches. The physical parameters for the PIC151 piezoelectric patches are given in Table D.1. Small screws attach the shim material to the end of the beam structure, as shown in Figures 2.5 and 2.7. The shim material are appropriately fastened at $L_{sh} = 5mm$ to a secure structure, i.e. a Newport RS3000 optical table with passive isolation structural supports. The optical table is used to lower ambient noise levels that may effect measurements, such as machinery noise and building transmission noise.

To validate the experimental boundary conditions, a Polytec Scanning Vibrometer (PSV-300) was used to observe the mode shape behavior. The vibrometer measures the two-dimensional distribution of vibration velocities on the basis of laser interferometry.

Figure 2.8: First mode, $\omega_1 = 20.63Hz$.

The PSV-300 system is used as a non-contact transducer to measure the velocity of many points on the resonant beam structure. A periodic chirp was generated using a Hewlett Packard 33120A function generator, the signal was amplified using a high voltage power amplifier and then applied to the piezoelectric actuator. The frequency responses were taken, relating the point velocity to the actuator voltage, i.e. $V_{el}(x,s)/V_a(s)$. Results from the area scans are displayed in Figures 2.8 to 2.12 for the first five resonant modes of the experimental simply supported beam.

From the area scans, the experimental simply supported beam shows good mode shape behavior. One observation that was observed was that the beam had added torsional dynamics at $306.6Hz$, as shown in Figure 2.11. The additional torsional dynamics are due to the orientation of the shim material and should not cause any real problems when designing different passive and semi-active control strategies.

2.6 Model Verification

For the design of passive and semi-active controllers, we are interested in a particular bandwidth. For obvious reasons, the infinite order models produced by the modal analysis technique is not suitable, as in Section 2.3. As an alternative, the displacement and voltage frequency responses are measured and used a finite order model (say $N = 5$), with the

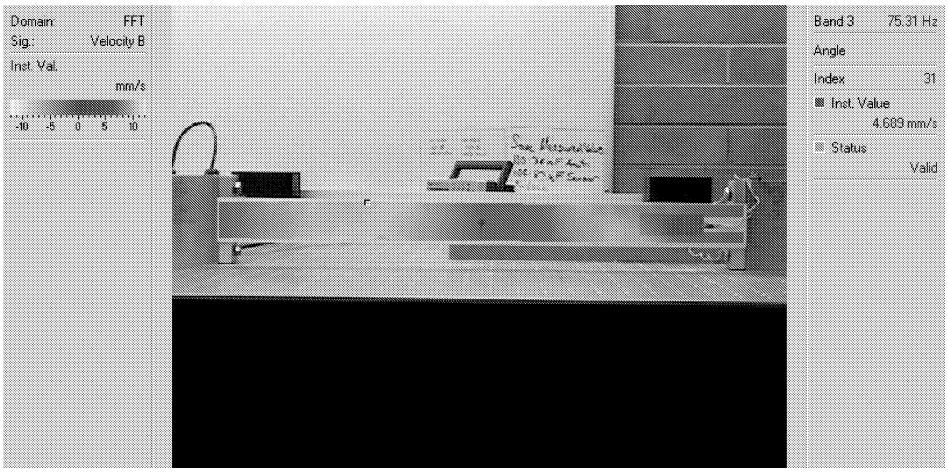

Figure 2.9: Second mode, $\omega_2 = 75.31Hz$.

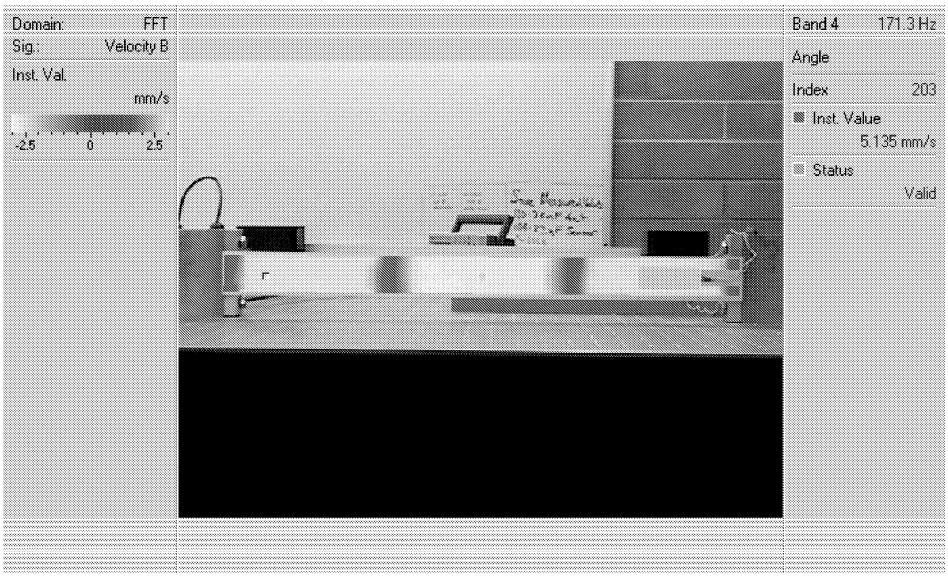

Figure 2.10: Third mode, $\omega_3 = 171.3Hz$.

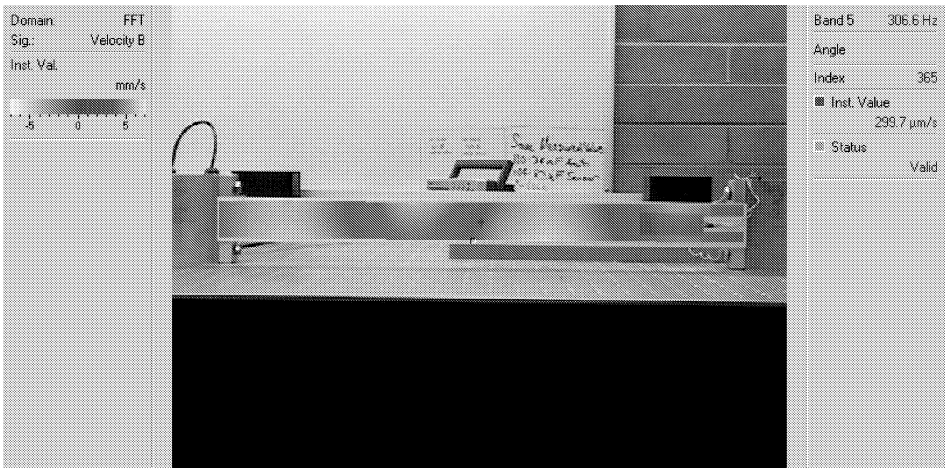

Figure 2.11: Fourth mode, $\omega_4 = 306.6Hz$.

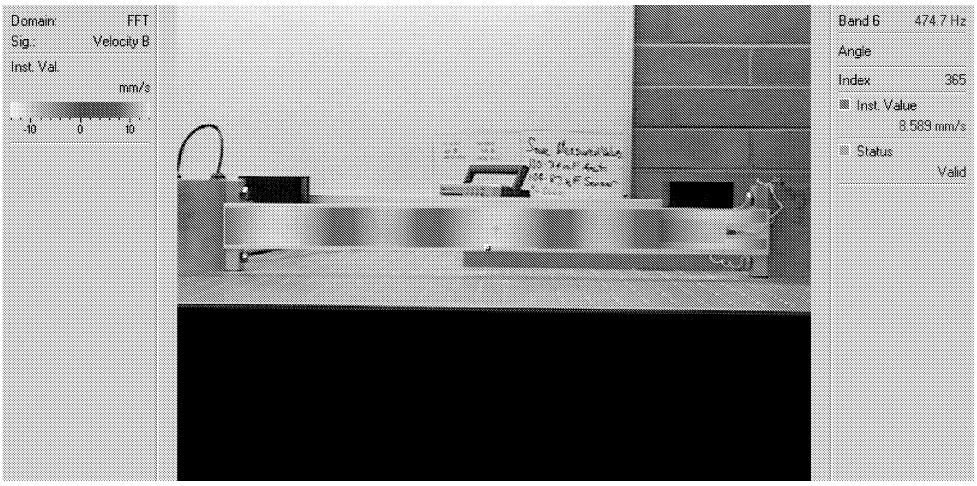

Figure 2.12: Fifth mode, $\omega_5 = 474.4Hz$.

following structure:

$$G_{yv}(x,s) = \frac{Y(x,s)}{V_a(s)} = \sum_{i=1}^{5} \frac{Fy_i}{s^2 + 2\zeta_i\omega_i s + \omega_i^2} + Ky_{opt}$$

and

$$G_{vv}(s) = \frac{V_s(s)}{V_a(s)} = \sum_{i=1}^{5} \frac{Fv_i}{s^2 + 2\zeta_i\omega_i s + \omega_i^2} + Kv_{opt},$$

where Ky_{opt} and Kv_{opt} are the zero frequency correction terms introduced in [17]. Although the truncated model can be found by minimizing the $\mathcal{H}_2$ norm of the additive error system [17], the inherent feedthrough term K_{opt} causes the corrected system to approach infinity[1]. To overcome this adverse effect, the corrected system $\left[\begin{array}{c|c} \mathbf{A}_c & \mathbf{B}_c \\ \hline \mathbf{C}_c & \mathbf{D}_c \end{array}\right]$ is remodeled with an additional parallel low pass filter $G_f(s) = \frac{\alpha}{s^2+2\zeta\omega_c s+\omega_c^2}$. If $\omega_c \gg \max(\omega_i)$ and $\frac{\alpha}{\omega_c^2} = K_{opt}$, the dynamics of the system in the bandwidth of interest are retained. The state-space realization becomes:

$$\left[\begin{array}{cc|c} \mathbf{A}_c & 0 & \mathbf{B}c \\ 0 & \mathbf{A}_f & \mathbf{B}_f \\ \hline \mathbf{C}_c & \mathbf{C}_f & 0 \end{array}\right] \Longrightarrow \left[\begin{array}{c|c} \mathbf{A} & \mathbf{B} \\ \hline \mathbf{C} & 0 \end{array}\right],$$

where $\left[\begin{array}{c|c} \mathbf{A}_f & \mathbf{B}_f \\ \hline \mathbf{C}_f & \mathbf{D}_f \end{array}\right]$ is the state space realization of the filter $G_f(s)$. Note that the feedthrough term $\mathbf{D}_c$ has been eliminated.

To validate the theoretical model with shim boundary conditions, experiments were carried out on the experimental piezoelectric laminated beam. The beam was excited using the piezoelectric actuator layer with a swept sine source from a Hewlett Packard 33120A function generator. The signal was then amplified using a high voltage power amplifier. A Hewlett Packard 35670A signal analyzer was used to measure the transfer function $G_{vv}(s)$, i.e. the voltage applied to the actuator to the shunting piezoelectric voltage. The displacement measurement is performed using a Polytec Laser Scanning Vibrometer. The $G_{yv}(x,s)$ transfer function was determined for a point on the composite structure located at $x_d = 0.170m$, as shown in Figure 2.1. The frequency response of the experimental system and identified model is shown in Figure 2.13. It is observed that the identified model is a good representation of the true system over the bandwidth of interest.*vs*

[1]This will become important in later chapters, as in Section 3.3, as we minimize the $\mathcal{H}_2$ norm of the passive dampened system.

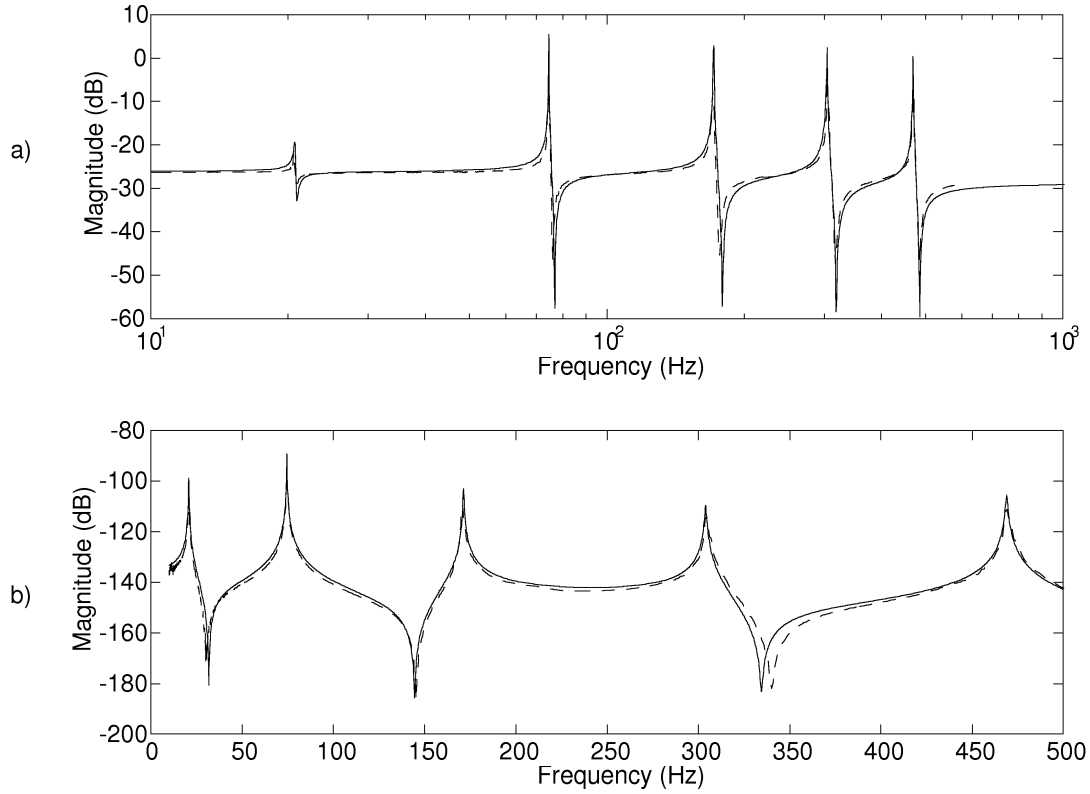

Figure 2.13: Frequency responses of a) $|G_{vv}(s)|$, b) $|G_{yv}(0.170, s)|$: experimental ($\cdots$) and modeled results (—).

Mode	**Ideal Model** (Hz)	**Model w/ SBC** (Hz)	**Experimental** (Hz)
1	18.72	19.89	20.63
2	74.85	74.52	74.61
3	168.43	171.4	171.3
4	299.43	304.9	306.6
5	467.87	468.5	474.4

Table 2.1: Model frequencies: mathematical models vs experimental results.

Mode	**Damping** (ζ)
1	0.0053
2	0.0014
3	0.0021
4	0.0017
5	0.0011

Table 2.2: Damping parameters determined experimentally.

The first five resonant frequencies $\omega_1, \ldots, \omega_5$ for the ideal boundary conditions, shim boundary conditions (SBC) and experimental results are tabulated in Table 2.1. The experimental damping values ζ, shown in Table 2.2, were measured using the Hewlett Packard 35670A signal analyzer and were incorporated into the state-space model. From the tabulated frequencies, we can see that the theoretical SBC model closely predicates the experimental results compared to the ideal pinned boundary conditions.

2.7 Chapter Conclusion

The application of the models derived in the chapter to a practical simply supported beam has been demonstrated. The models derived here are now used to design passive and semi-active controllers to improve the damping of the resonant system.

Chapter 3

Passive Shunt Damping

Shunt damping methodologies are often grouped into three broad categories: resistive, single mode and multiple modes. Resistive shunt dampens the structure but the performance is limited. Single mode shunt damping techniques are simple but damp only one structural mode for every piezoelectric element. Multiple mode shunt damping techniques require more complicated shunt circuits but are capable of damping several modes.

3.1 Introduction

3.1.1 Resistive Shunt Damping

When a simple resistor is placed across the terminals of a piezoelectric element, the piezoelectric damper will act as a viscoelastic damper [13]. The resistor provides a means of energy dissipation, i.e. increases the mechanical loss factor. This type of damper has limited performance. The optimal damping resistance depends on the specific damping frequency, mechanical coupling coefficients and the inherent capacitance of the piezoelectric element. For further reading the reader is referred to [13].

3.1.2 Single Mode Shunt Damping

Single mode damping was introduced to decrease the magnitude of one structural mode [13]. Two examples of single mode damping are shown in Figure 3.1, parallel [27] and series shunt damping [13]. Using the inherent capacitance of the piezoelectric, a $R-L$ shunt circuit introduces an electrical resonance. This can be tuned to one structural mode in a manner

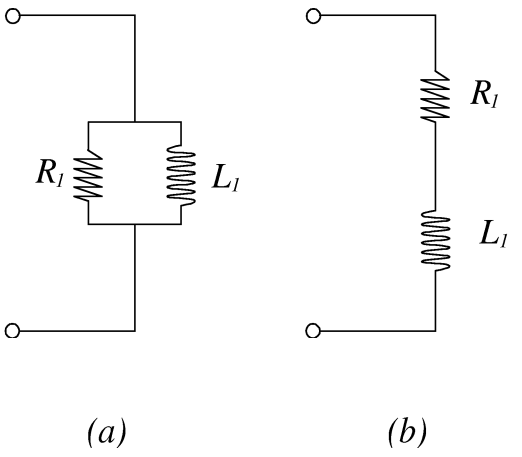

Figure 3.1: Examples of single mode shunt circuits: (a) parallel case and (b) series case.

analogous to a mechanical vibration absorber [13]. Single mode damping can be applied to reduce vibration due to several structural modes with the use of as many piezoelectric patches and damping circuits. The optimal damping resistance R_1 depends on the specific damping frequency, mechanical coupling coefficients and the inherent capacitance of the piezoelectric element [13, 27].

Problems may arise if these piezoelectric patches are bonded to or embedded in the structure. First, the structure may not have sufficient room to accommodate all of the patches. Second, if there is insufficient room, the structure may be altered or weakened when the piezoelectric patches are applied. In addition, a large number of patches can increase the structural weight, making it unsuitable for applications such as aerospace systems.

3.1.3 Multiple Mode Shunt Damping

To alleviate the problems associated with single mode damping, multi-mode shunt damping has been introduced, i.e. the use of one piezoelectric patch to damp several structural modes. There are two common circuit configurations for multi-mode shunt damping and they are called parallel and series cases. Examples of these two configurations are shown in Figure 3.2. There are other examples of multi-mode shunt damping but these will not be discussed in this thesis.

The principle of multi-mode shunt damping is to insert a "current blocking" or an-

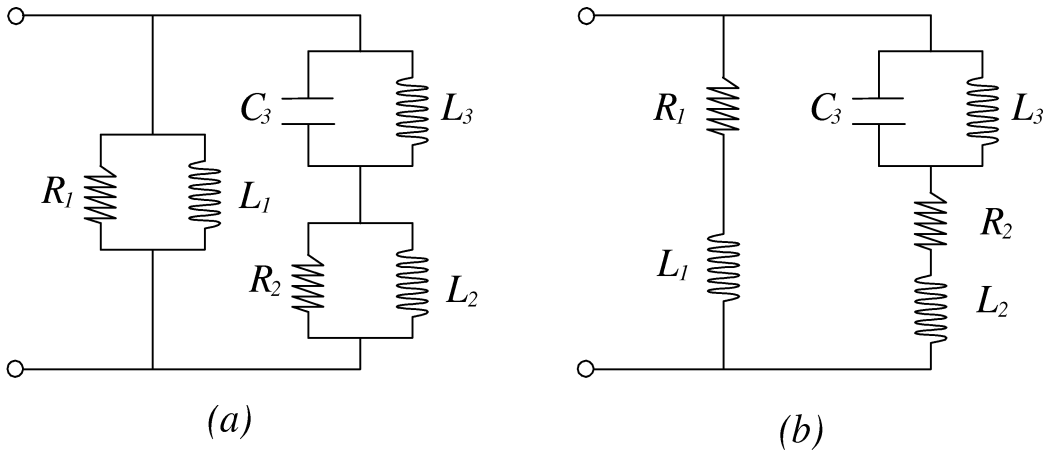

Figure 3.2: Examples of multiple mode shunt circuits: (a) parallel case [28] and (b) series case.

tiresonance circuit [27, 28, 29, 30] in series with each shunt branch. In Figure 3.2, the blocking circuit consists of a capacitor and inductor in parallel, $C_3 - L_3$. The number of antiresonance circuits in each $R - L$ shunt branch depends on the number of structural modes to be damped simultaneously. Each $R-L$ shunt branch is designed to dampen only one structural mode. For example, $R_1 - L_1$ in Figure 3.2 is tuned to resonate at ω_1, the resonant frequency of the first structural mode to be damped. $R_2 - L_2$ is tuned to ω_2, the second structural mode to be damped, and so on.

According to Wu [28], the inductance values for the shunt circuits shown in Figure 3.2 (a) and (b) can be calculated from the following expressions. It is assumed that $\omega_1 < \omega_2$.

$$L_1 = \frac{1}{\omega_1^2 C_p} \tag{3.1}$$

and

$$L_2 = \frac{\left(L_1\tilde{L}_2 + \tilde{L}_2 L_3 - L_1 L_3 - \omega_2^2 L_1 \tilde{L}_2 L_3 C_3\right)}{\left(L_1 - \tilde{L}_2\right)\left(1 - \omega_2^2 L_3 C_3\right)}, \tag{3.2}$$

where

$$\tilde{L}_2 = \frac{1}{\omega_2^2 C_p} \tag{3.3}$$

and

$$L_3 = \frac{1}{\omega_1^2 C_3}. \tag{3.4}$$

C_p is the capacitance of the piezoelectric element and C_3 is an arbitrary capacitor used in the current blocking network.

Current techniques for determining the resistive elements for shunt damping are based on rather ad-hoc methodologies [9, 12, 14, 27, 28, 29, 30]. Even though this technique for determining the resistance values (R_1 and R_2) is reliable and the complete circuit can be fine-tuned by trial and error [9, 12, 14, 27, 28, 29, 30], there are two important questions that need to be addressed when applying multiple mode shunt damping. The first question is how the shunt resistive values required for optimal multi-mode shunting should be calculated. The second question is why the parallel shunt damping case presented in [27, 28, 29, 30] is easier to implement practically than the series shunting circuit [9, 12, 14]. It is, therefore, the aim of this chapter to present answers to these two questions.

3.2 Dynamic Model of the Composite System

As discussed in Section 3.1.3, there are two common circuit configurations used for multi-mode shunt damping and they are called series and parallel cases, as shown in Figure 3.2. In order to model the presence of the shunt network, the coupled terminal dynamics of the circuit and laminated beam are considered.

Piezoelectric transducers behave electrically like a capacitor C_p and mechanically like a stiff spring. It is common to model the piezoelectric element as a capacitor C_p in series with a strain dependent voltage source [8, 13]. Consider Figures 2.1 and 3.3, where a piezoelectric patch is shunted with an impedance Z. The current-voltage relation of the impedance can be represented in state-space form as

$$\dot{\mathbf{x}}_z = \mathbf{A}_z \mathbf{x}_z + \mathbf{B}_z V_z \tag{3.5}$$

and

$$i_z = \mathbf{C}_z \mathbf{x}_z + \mathbf{D}_z V_z, \tag{3.6}$$

where V_z is the voltage across the impedance and i_z is the current flowing through the circuit. The relationship between V_z and V_p, shown in Figures 2.1 and 3.3, is

$$\dot{\mathbf{x}}_b = \mathbf{A}\mathbf{x}_b + \mathbf{B} V_z, \tag{3.7}$$

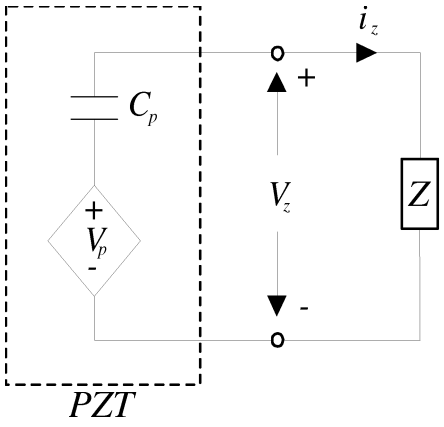

Figure 3.3: Shunt piezoelectric element schematic.

and

$$V_p = -\mathbf{C}_{V_s}\mathbf{x}_b \tag{3.8}$$

where V_p is the voltage induced from the electromechanical coupling effect. By shunting the piezoelectric patch, the voltage V_z across the shunting layer or impedance, shown in Figure 3.3, is related to the terminal voltage and current by

$$V_z = V_p - \frac{1}{C_p}\int i_z dt.$$

The variable i_z can be replaced with $\dot{\mathbf{q}}_z$, the charge on the piezoelectric patch. Consequently, by replacing V_z and substituting $V_p = -\mathbf{C}_{V_s}\mathbf{x}_b$, (3.5), (3.6) and (3.7) becomes

$$\dot{\mathbf{x}}_b = (\mathbf{A} - \mathbf{B}\mathbf{C}_{V_s})\mathbf{x}_b - \frac{1}{C_p}\mathbf{B}\mathbf{q}_z. \tag{3.9}$$

For the variable $\dot{\mathbf{x}}_z$, it can be shown that

$$\dot{\mathbf{x}}_z = \mathbf{A}_z\mathbf{x}_z - \mathbf{B}_z\mathbf{C}_{V_s}\mathbf{x}_b - \frac{1}{C_p}\mathbf{B}_z\mathbf{q}_z \tag{3.10}$$

and thus $\dot{\mathbf{q}}_z$ is

$$\dot{\mathbf{q}}_z = \mathbf{C}_z\mathbf{x}_z - \mathbf{D}_z\mathbf{C}_{V_s}\mathbf{x}_b - \frac{1}{C_p}\mathbf{D}_z\mathbf{q}_z. \tag{3.11}$$

The combination of (3.9), (3.10) and (3.11) leads to the following state-space representation,

$$\begin{bmatrix} \dot{\mathbf{x}}_b \\ \dot{\mathbf{x}}_z \\ \dot{\mathbf{q}}_z \end{bmatrix} = \begin{bmatrix} \mathbf{A} - \mathbf{B}\mathbf{C}_{V_s} & \mathbf{0} & -\frac{1}{C_p}\mathbf{B} \\ -\mathbf{B}_z\mathbf{C}_{V_s} & \mathbf{A}_z & -\frac{1}{C_p}\mathbf{B}_z \\ -\mathbf{D}_z\mathbf{C}_{V_s} & \mathbf{C}_z & -\frac{1}{C_p}\mathbf{D}_z \end{bmatrix} \begin{bmatrix} \mathbf{x}_b \\ \mathbf{x}_z \\ \mathbf{q}_z \end{bmatrix}. \tag{3.12}$$

If a voltage V_a is applied to the piezoelectric actuator, then (3.12) becomes

$$\begin{aligned} \dot{\mathbf{X}} &= \tilde{\mathbf{A}}\mathbf{X} + \tilde{\mathbf{B}}V_a \\ V_z &= \tilde{\mathbf{C}}_{V_s}\mathbf{X} \\ Y &= \tilde{\mathbf{C}}_Y\mathbf{X}, \end{aligned} \tag{3.13}$$

where $\mathbf{X} = \begin{bmatrix} \mathbf{x}_b & \mathbf{x}_z & \mathbf{q}_z \end{bmatrix}^T$, $\tilde{\mathbf{B}} = \begin{bmatrix} \mathbf{B} & \mathbf{0} & \mathbf{0} \end{bmatrix}^T$, $\tilde{\mathbf{C}}_{V_s} = \begin{bmatrix} \mathbf{C}_{V_s} & \mathbf{0} & \mathbf{0} \end{bmatrix}^T$, $\tilde{\mathbf{C}}_Y = \begin{bmatrix} \mathbf{C}_Y & \mathbf{0} & \mathbf{0} \end{bmatrix}^T$ and

$$\tilde{\mathbf{A}} = \begin{bmatrix} \mathbf{A} - \mathbf{B}\mathbf{C}_{V_s} & \mathbf{0} & -\frac{1}{C_p}\mathbf{B} \\ -\mathbf{B}_z\mathbf{C}_{V_s} & \mathbf{A}_z & -\frac{1}{C_p}\mathbf{B}_z \\ -\mathbf{D}_z\mathbf{C}_{V_s} & \mathbf{C}_z & -\frac{1}{C_p}\mathbf{D}_z \end{bmatrix}.$$

We now have the state-space representation of $V_z(s)/V_a(s)$ and $Y(x,s)/V_a(s)$ for a single input single output (SISO) system. During the course of the thesis, $Y(x,s)/V_a(s)$ is of most interest, since we want to minimize the vibration at a point on the beam structure. By minimizing the vibration at a point, we are minimizing the energy of the resonant system.

3.3 Determining the Shunting Resistances via Optimization

In order to find appropriate values for the shunt resistors $\mathbf{R} = \{R_1, R_2, ..., R_n\}$, an optimization approach is proposed. A set of resistors can be found so that the $\mathcal{H}_2$ norm of the damped system is minimized. Minimizing the $\mathcal{H}_2$ norm of the system minimizes the RMS displacement at a single or series of points due to a spectrally white disturbance signal applied to the actuator(s).

3.3.1 Optimization Technique

Consider a transfer function matrix $\tilde{\mathbf{G}}(s) \in \mathbb{C}^{m\times n}$ representing the damped system (3.13). The $\mathcal{H}_2$ norm of $\tilde{\mathbf{G}}(s)$, denoted $\left\|\tilde{\mathbf{G}}(s)\right\|_2$, is defined as:

$$\left\|\tilde{\mathbf{G}}(s)\right\|_2^2 = \frac{1}{2\pi}\int_{-\infty}^{\infty} tr\left(\tilde{\mathbf{G}}^T(-j\omega)\tilde{\mathbf{G}}(j\omega)d\omega\right).$$

Let $\tilde{\mathbf{G}}(s)$ have the realization $\tilde{\mathbf{G}}(s) = \tilde{\mathbf{C}}(s\mathbf{I} - \tilde{\mathbf{A}})^{-1}\tilde{\mathbf{B}}$. If the matrix $\tilde{\mathbf{A}}$ is stable, the following equality holds

$$J = \|\mathbf{G}(s)\|_2^2 = tr(\tilde{\mathbf{C}}\mathbf{P}\tilde{\mathbf{C}}^T), \tag{3.14}$$

where $\mathbf{P}$ satisfies the *Lyapunov* equation $\tilde{\mathbf{A}}^T\mathbf{P} + \mathbf{P}\tilde{\mathbf{A}} + \tilde{\mathbf{B}}\tilde{\mathbf{B}}^T = \mathbf{0}$. In this case $\tilde{\mathbf{A}}$ is a function of $\mathbf{R}$. This leads to the following constrained optimization problem:

$$\mathbf{R}^* = \arg\min_{s.t.\ \mathbf{g}=\mathbf{0}} J, \tag{3.15}$$

where $\mathbf{g} = \tilde{\mathbf{A}}^T\mathbf{P} + \mathbf{P}\tilde{\mathbf{A}} + \tilde{\mathbf{B}}\tilde{\mathbf{B}}^T$ and $\mathbf{R} = \{R_1, R_2, ..., R_n\} > 0$.

Having set up the optimization problem (3.15), a number of methods can be employed to find an optimal set of resistors $\mathbf{R}^* = \{R_1^*, R_2^*, ..., R_n^*\}$. One such method is the Nelder-Mead simplex search algorithm. A more elegant and computationally efficient method of solving (3.15) is to use the gradient search algorithm. By introducing the matrix of Lagrange multipliers $\mathbf{S}$, the Lagrangian L is formed as follows

$$L = tr(\tilde{\mathbf{C}}\mathbf{P}\tilde{\mathbf{C}}^T) + tr(\mathbf{g}\mathbf{S}).$$

The first order necessary conditions for optimality are found by equating the derivatives of L with respect to the parameters $\mathbf{P}$, $\mathbf{S}$ and $\mathbf{R}$ to zero:

$$\frac{\partial L}{\partial \mathbf{S}} = \tilde{\mathbf{A}}\mathbf{P} + \mathbf{P}\tilde{\mathbf{A}}^T + \tilde{\mathbf{B}}\tilde{\mathbf{B}}^T = \mathbf{0}, \tag{3.16}$$

$$\frac{\partial L}{\partial \mathbf{P}} = \tilde{\mathbf{A}}^T\mathbf{S} + \mathbf{S}\tilde{\mathbf{A}} + \tilde{\mathbf{C}}^T\tilde{\mathbf{C}} = \mathbf{0}, \tag{3.17}$$

$$\frac{\partial L}{\partial R_1} = tr\left(\tilde{\mathbf{E}}_1\mathbf{P}\mathbf{S} + \mathbf{P}\tilde{\mathbf{E}}_1^T\mathbf{S}\right) = 0,$$

$$\vdots$$

$$\frac{\partial L}{\partial R_n} = tr\left(\tilde{\mathbf{E}}_n\mathbf{P}\mathbf{S} + \mathbf{P}\tilde{\mathbf{E}}_n^T\mathbf{S}\right) = 0. \tag{3.18}$$

With n resistors, $\tilde{\mathbf{A}}$ can be represented as $\tilde{\mathbf{A}} = \bar{\mathbf{A}} + R_1\tilde{\mathbf{E}}_1 + ... + R_n\tilde{\mathbf{E}}_n$, where $\bar{\mathbf{A}}$ is independent of $\mathbf{R}$.

The $\mathcal{H}_2$ norm of the system can now be minimized by solving the above equations simultaneously. It is not possible to obtain a closed form solution, so a numerical approach is required.

As preliminaries for the optimization, the static matrices ($\tilde{\mathbf{B}}$ and $\tilde{\mathbf{C}}$) are computed and an initial estimate $\mathbf{R}_0$ is made for $\mathbf{R}^*$. Matrix $\tilde{\mathbf{A}}$ is a function of $\mathbf{R}_k$ and is updated at each iteration. Matrices $\mathbf{P}$ and $\mathbf{S}$ are calculated by solving the Lyapunov equations (3.16) and (3.17)**.** The direction of steepest descent is found by evaluating the gradient vector, whose entries are the partial derivatives of L with respect to $R_1, R_2, ..., R_n$ (3.18). The process is iterated by updating $\mathbf{R}_k$ until a minima is obtained (i.e. until the exiting conditions $\frac{\partial L}{\partial R_i} \approx 0$ and $L_{k+1} \approx L_k$ are satisfied). Since the problem is not convex, an iterative optimization procedure can be carried out for a number of initial guesses to obtain the best solution.

3.4 Experimental Verification

To validate the optimal shunt damping concept, experiments were carried out on the simply supported piezoelectric laminated beam. The experimental setup was introduced in Section 2. Two different multi-mode shunt circuits were examined and they are: (a) the parallel shunt circuit; and (b) the series shunt circuit, as shown in Figure 3.2. Also, for simplicity, only the $2nd$ ($\omega_1 = 74.5Hz$) and $3rd$ ($\omega_2 = 171.3Hz$) structural modes of the piezoelectric composite beam were considered for shunting. The $2nd$ and $3rd$ structural modes were chosen due to their high resonant amplitudes, as shown in Figure 2.13. The reason for only considering the $2nd$ and $3rd$ mode is because these modes have more authority in comparison to other structural modes due to the chosen location of the piezoelectric patch.

According to [28], the inductance L_1, L_2 and L_3 of these two circuits are defined in equations (3.1) to (3.4). Both parallel and series circuit cases were designed under the assumption that $\omega_1 < \omega_2$. The "blocking" capacitance C_3 was chosen to be $100nF$ because of the commercial availability of these capacitors. The inductor parameters were found to be $L_1 = 43H$, $L_2 = 20.9H$ and $L_3 = 45.2H$. Using the already mentioned circuit parameters for the shunt and dynamic composite modeling method, the $\mathcal{H}_2$ norm of the composite system was minimized. The optimal resistance values for R_1 and R_2, for both the parallel and series shunt cases, are obtained. Figures 3.4 and 3.5 show the $\mathcal{H}_2$ norm cost surface as a function of R_1 and R_2.

From Figures 3.4 and 3.5, it can be seen that both cost surfaces have a minimum. For the parallel shunt case, the optimal region is larger than the one for the series shunt case.

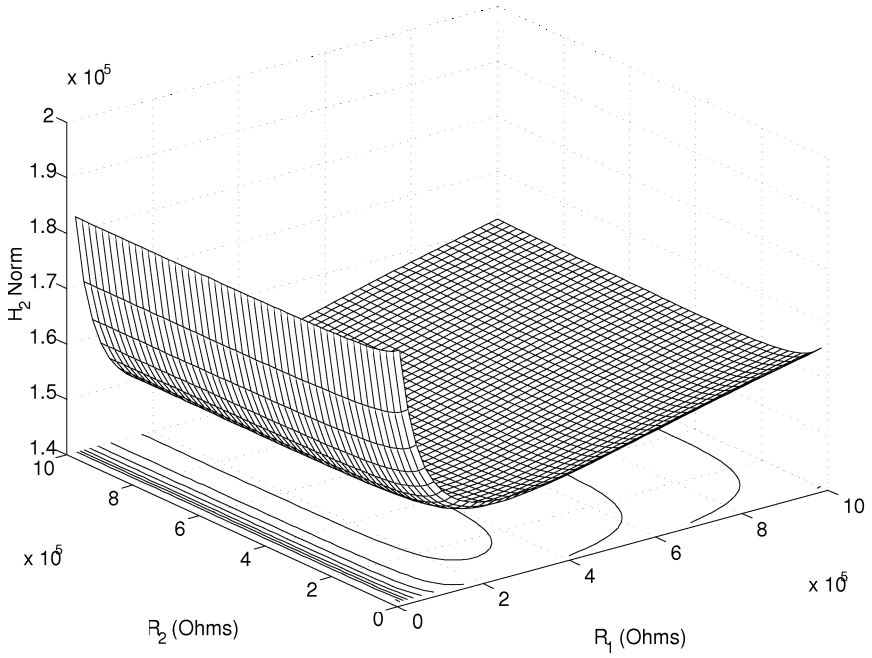

Figure 3.4: Parallel case: $G_{yv}(0.170, s)$ $\mathcal{H}_2$ norm cost surface as a function of R_1 and R_2.

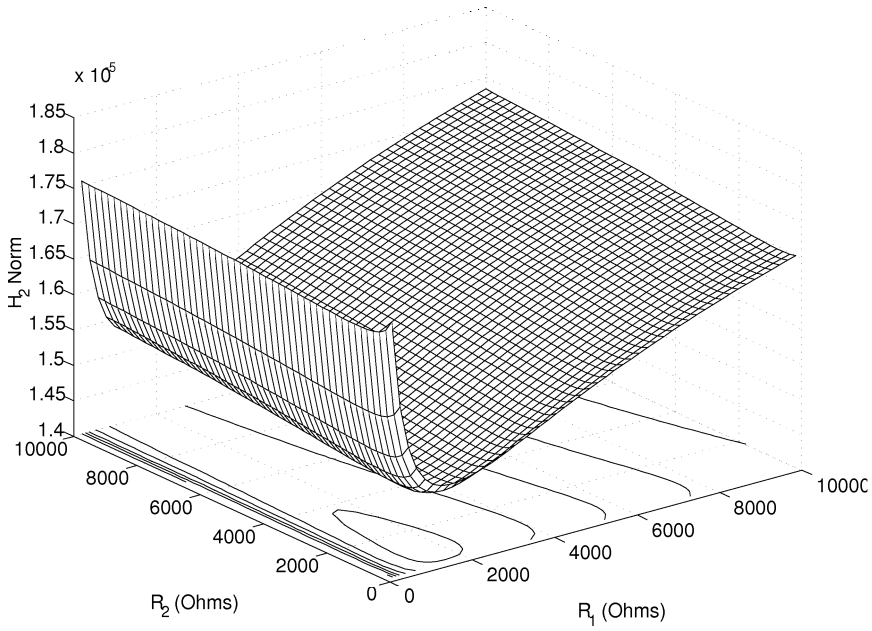

Figure 3.5: Series case: $G_{yv}(0.170, s)$ $\mathcal{H}_2$ norm cost surface as a function of R_1 and R_2.

This justifies the work presented in [27], which states that *"the parallel shunt circuit is therefore easier and more practical"*, i.e. the parallel shunt case is less sensitive to circuit tuning compared with the series case.

The optimization algorithm found a minimum at $R_1^* = 262.75k\Omega$ and $R_2^* = 550.73k\Omega$ for the parallel shunt case, while the minimum for the series shunt case was found to be at $R_1^* = 1543.4\Omega$ and $R_2^* = 1145.2\Omega$.

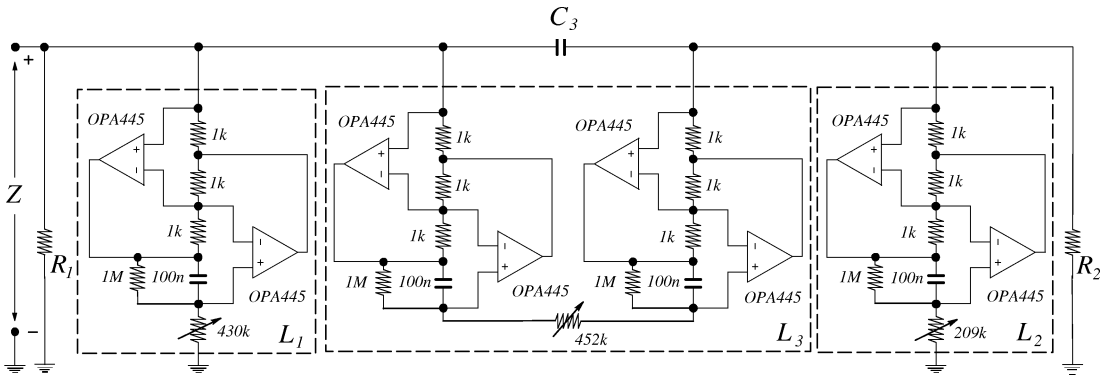

Figure 3.6: Experimental parallel shunt circuit for R_1, R_2, L_1, L_2, L_3 and C_3.

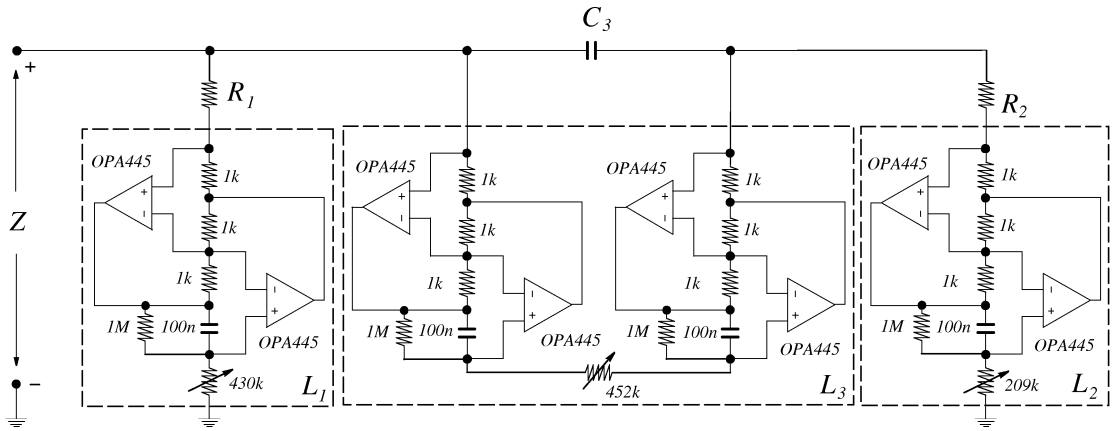

Figure 3.7: Experimental series shunt circuit for R_1, R_2, L_1, L_2, L_3 and C_3.

Parameters L_1, L_2, L_3 and C_3 were then employed in the design of the two shunt circuits, parallel and series (refer to Figures 3.6 and 3.7) shunt cases, and then tested across the piezoelectric patch. Construction of the shunt circuits requires Riordan high Q factor simulated floating/grounded inductors [22] for L_1, L_2 and L_3. A summary about ground/floating inductors can be found in Appendix A. Burr-Brown OPA445 operational amplifiers were used to construct the inductor circuits. These operational amplifiers have a supply voltage limit of ± 45 v.

To justify the $\mathcal{H}_2$ norm optimization technique, the magnitude frequency response were taken for the $G_{yv}(0.170, s)$ before and after shunt damping at $x_d = 0.170m$. Figure 3.8 shows the results for the parallel and series circuit cases respectively.

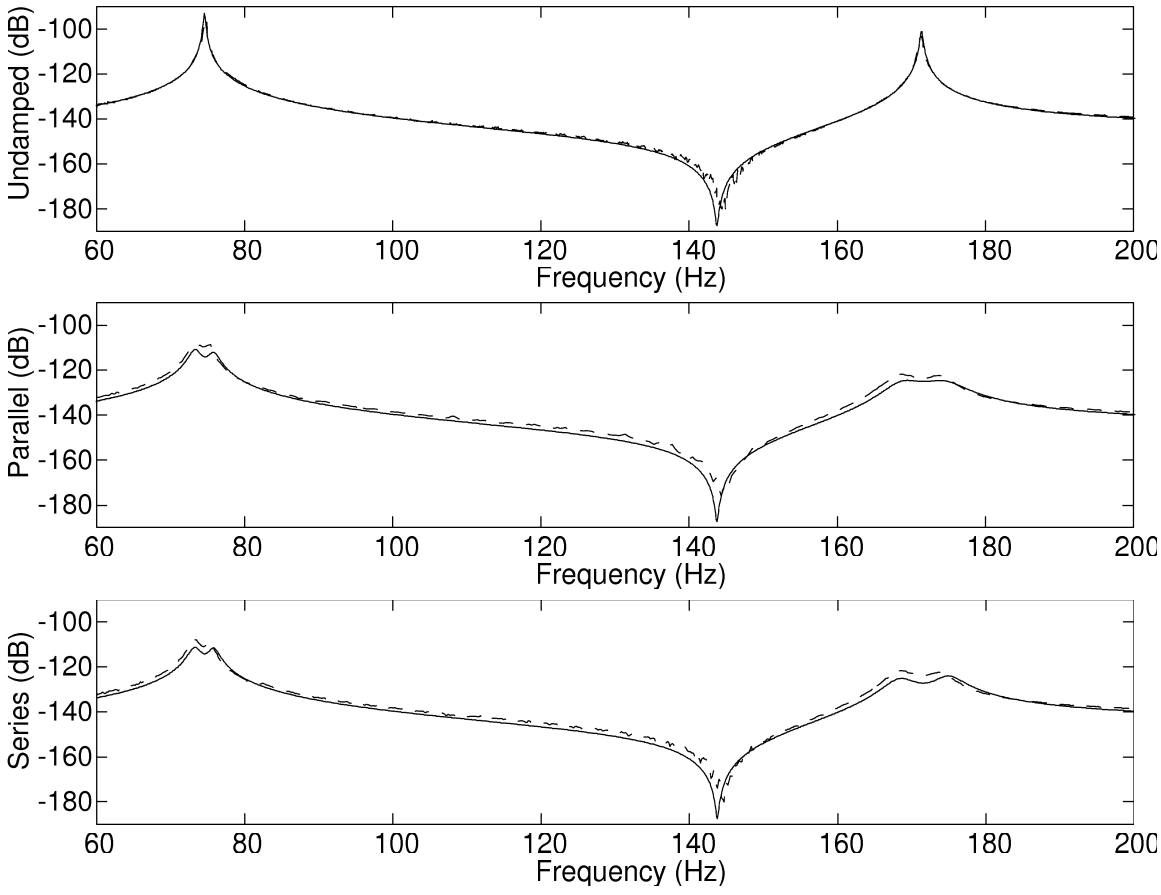

Figure 3.8: Parallel and series shunt circuit cases of $|G_{yv}(0.170, s)|$: theoretical (—) and experimental results ($\cdots$).

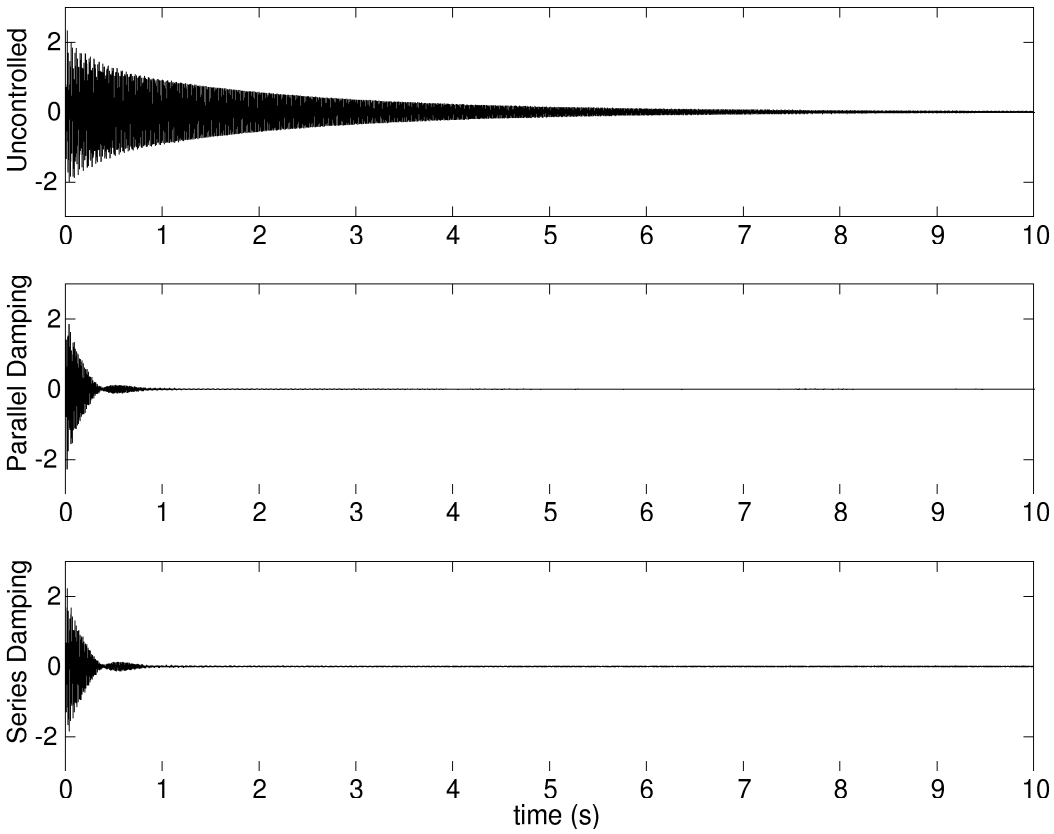

Figure 3.9: Experimental time responses, $V_{el}(0.170, s)/V_a(s)$.

After tuning the shunt resistances, the following experimental values were found: in the parallel multi-mode shunt case $R_1 = 246.3k\Omega$ and $R_2 = 540.2k\Omega$; and in the series multi-mode shunt case $R_1 = 935.2\Omega$ and $R_2 = 732.1\Omega$. Comparing resistors obtained from experimental results with these obtained from theoretical results, it can be seen that the experimental tuned values are near to the predicated theoretical optimal values. Figure 3.8 shows the magnitude results for $G_{yv}(0.170, s)$, in the parallel and series circuit cases respectively.

The experimental resonant amplitudes for the $2nd$ and $3rd$ modes were successfully reduced for both the parallel and series cases. The parallel resonant amplitudes were reduced by $18.9dB$ and $19.1dB$. For the series case, a reduction of $18.7dB$ and $19.2dB$ was obtained. From theoretical simulations the resonant amplitudes at $2nd$ and $3rd$ modes for the both parallel and series circuit cases were $21.6dB$ and $21.1dB$; and $21.5dB$ and $21.2dB$.

	Parallel Case ($k\Omega$)		**Series Case** (Ω)	
Mode	Simulated	Experimental	Simulated	Experimental
R_1	262.75	246.3	1543.4	935.2
R_2	550.73	540.2	1145.2	732.1

Table 3.1: Summary of resistance damping elements.

	Parallel Case (dB)		**Series Case** (dB)	
Mode	Simulated	Experimental	Simulated	Experimental
$2nd$	21.6	18.9	21.5	18.7
$3rd$	21.1	19.1	21.2	19.2

Table 3.2: Summary of magnitude reduction results.

	Parallel Case	**Series Case**
$\frac{\text{Undamped Settling Time}}{\text{Damped Settling Time}}$	$\frac{1}{10}$	$\frac{1}{10}$

Table 3.3: Summary of experimental time results.

To complete the validation, a second set of experimental data was taken to test the proposed optimal approach in a transient regime. The experiment consisted of exciting the beam structure using a step voltage across the piezoelectric actuator and monitoring the velocity decay at a point on the beam structure, $V_{el}(0.170, s)/V_a(s)$. A Polytec Laser Scanning Vibrometer (PSV-300) was used to monitor the velocity decay at a point at $x_d = 0.170m$. The rapid prototype system, dSpace, was used to generate the voltage step and capture the time response data from the vibrometer. The sampling frequency was set at $20kHz$. Within dSpace, a low-pass digital filter was used to remove high order structural modes and noise. The cut-off frequency for the digital filter was set at $230Hz$. After sampling the time response, the data was filtered with a high-pass digital filter to remove low frequency noise. The cut-off frequency was chosen to be $30Hz$ so as to remove the dynamics of the $1st$ structural mode. Results from the transient time regime are shown in Figure 3.9.

A summary of the optimal resistive values, magnitude reduction results and experimental time results are shown in Tables 3.1, 3.2 and 3.3 respectively.

3.5 Chapter Conclusion

From this chapter, we have developed a systematic way of determining the required optimal damping resistance for multiple mode shunts. Two different multi-mode shunt damping techniques were examined, namely the parallel [28] and series cases. A state-space theoretical model of the dampened system was also developed. Damped theoretical results were found to closely agree with experimental results.

Chapter 4

Synthetic Impedance

4.1 Introduction

Currently shunt damping circuits are implemented using a network of physical components, as shown in Figures 3.6 and 3.7. There are a number of problems associated with this *direct circuit* implementation, the foremost of which are listed below.

1. Typically shunt circuits require large inductor values (up to thousands of Henries). Virtual grounded/floating inductors (Riordan Gyrators [22]) are required to implement the inductor elements. Such virtual implementations are typically poor representations of ideal inductors. They are large in size, difficult to tune and are sensitive to component age, temperature and non-ideal characteristics.

2. Piezoelectric patches are capable of generating hundreds of volts for moderate structural excitations. This requires the entire circuit to be constructed from high voltage components. Furthermore, voltage limitations arise due to the internal gains of the virtual inductors.

3. The minimum number of operational amplifiers required to implement the shunt damping circuit increases rapidly with the number of modes to be damped. At least 30 operational amplifiers are required to implement a series configuration multi-mode shunt damping circuit with a "current blocker" in every branch. The relationship between the number of operational amplifiers and the number of modes to be damped for this circuit configuration is given by $2n + 4n(n-1)$, where n is the number of modes to be damped.

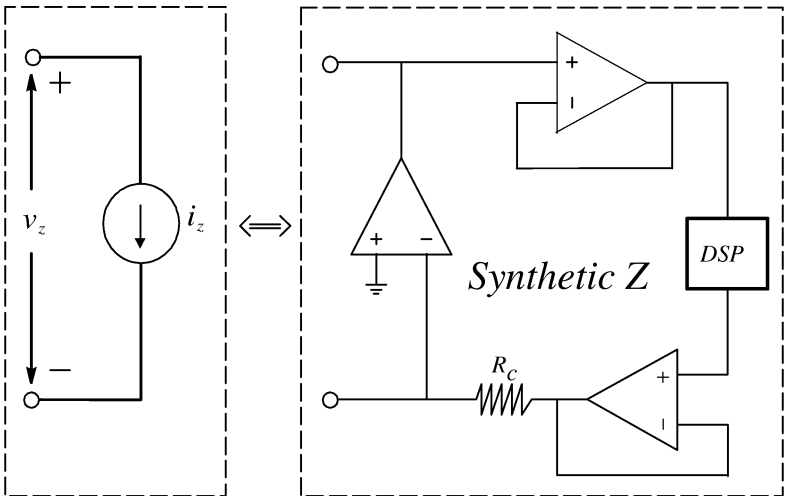

Figure 4.1: Current source implementation.

4.2 Implementation of Shunt Damping Circuits

It should be clear from the previous section that the concept of multi-mode shunt damping is useful, but implementation difficulties make its application somewhat limited. This section introduces a new method of implementing an arbitrary shunt impedance, namely the "synthetic impedance" using a voltage controlled current source and a digital signal processor (DSP).

4.2.1 The Synthetic Impedance

We define a "synthetic impedance" as a two terminal device that establishes an arbitrary relationship between voltage and current at its terminals. The functionality is shown in Figure 4.1, where $i_z(t) = f(v_z(t))$. This can be made to synthesize any network of physical components by fixing i_z to be the output of a linear transfer function of v_z, i.e.

$$I_z(s) = Y(s)V_z(s), \tag{4.1}$$

where $Y(s) = \frac{1}{Z(s)}$ and $Z(s)$ is the impedance to be seen from the terminals.

4.2.2 Circuit Diagram / Transfer Function Equivalence

In Section 4.2.1, $Y(s)$ is formed analytically by calculating the complex admittance of the network. In practical situations where there may be a large number of shunt circuit elements, it is desirable to "redraw" the circuit as a transfer function block diagram so that the overall $\frac{output(s)}{input(s)}$ relationship is equal to $Y(s)$. This can simplify the process of writing DSP algorithms. Moreover, if a graphical compilation package such as the Real Time Workshop (RTW) for MATLAB is available, the need for any transfer function derivations or algorithm coding is removed.

Two transformations of interest are shown in Figures 4.2 and 4.3. These can be combined to find an equivalent transfer function form for any network of impedances.

Parallel circuit equivalence. Consider the parallel network components $Z_1, Z_2, \ldots,$ Z_m as shown in Figure 4.2. The terminal impedance and admittance of this network are:

$$Z_T(s) = (\frac{1}{Z_1} + \frac{1}{Z_2} + \ldots + \frac{1}{Z_m})^{-1}$$

and

$$Y_T(s) = \frac{1}{Z_1} + \frac{1}{Z_2} + \ldots + \frac{1}{Z_m}. \tag{4.2}$$

Now consider the transfer function block diagram, also shown in Figure 4.2.

$$G(s) = \frac{T(s)}{R(s)} = \frac{1}{Z_1} + \frac{1}{Z_2} + \ldots + \frac{1}{Z_m} \tag{4.3}$$

It is noted that $Y_T(s)$ and $G(s)$, as described in equations (4.2) and (4.3) are identical. Therefore, if a synthetic impedance as shown in Figure 4.3 is implemented with a transfer function equal to $G(s)$, the impedance seen from the terminals will be identical to the impedance of the parallel network shown in Figure 4.2 (with impedance $Z_T(s)$ given by (4.2)).

Series circuit equivalence. Consider the series network components $Z_1, Z_2, \ldots, Z_m$ as shown in Figure 4.3. The terminal impedance and admittance of this network are:

$$Z_T(s) = Z_1 + Z_2 + \ldots + Z_m$$

and

$$Y_T(s) = \frac{1}{Z_1 + Z_2 + \ldots + Z_m}. \tag{4.4}$$

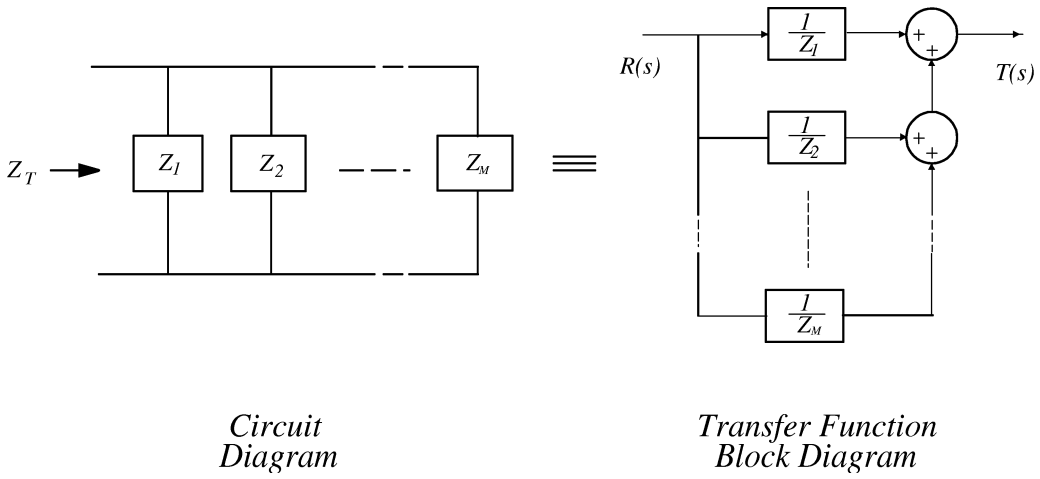

Figure 4.2: Parallel block equivalence.

Now consider the transfer function block diagram, also shown in Figure 4.3.

$$\begin{aligned} G(s) &= \frac{T(s)}{R(s)} = \frac{\frac{1}{Z_1}}{1 + \frac{1}{Z_1}Z_2 + \ldots + \frac{1}{Z_1}Z_m} \\ G(s) &= \frac{1}{Z_1 + Z_2 + \ldots + Z_m} \end{aligned} \tag{4.5}$$

It is noted that $Y_T(s)$ and $G(s)$, as described in equations (4.4) and (4.5), are identical. Therefore, if a synthetic impedance as shown in Figure 4.3 is implemented with a transfer function equal to $G(s)$, the impedance seen from the terminals will be identical to the impedance of the series network shown in Figure 4.3 (with impedance $Z_T(s)$ given by (4.4)).

4.3 Experimental Results

To assess the merit of the concepts presented, a number of experiments were carried out on a simple test circuit and the simply supported piezoelectric laminate beam. An experimental test circuit will be used to validate the proposed synthetic impedance device. Finally, the optimal multi-mode parallel and series shunt circuits (see Section 3.3.1) are synthesized and applied to the structure. Damping performance is evaluated by measuring the free and damped frequency responses of the beam.

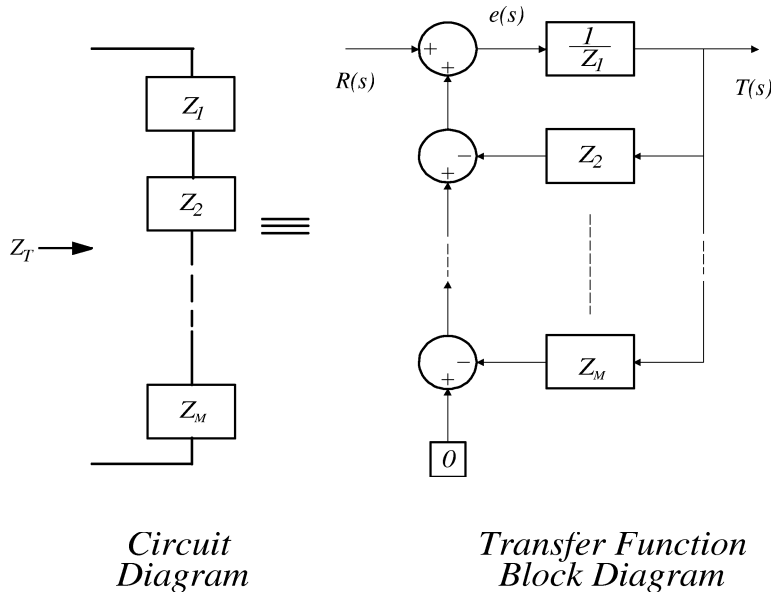

Figure 4.3: Series block equivalence.

4.3.1 Synthesis of Impedance

The implementing circuit is similar to the example implementation shown in Figure 4.1. A voltage controlled current source constructed from a single operational amplifier is used together with buffer/amplifiers and a DSP system to simulate impedance. The two unity gain buffers are replaced with non-inverting amplifiers of gain $\frac{1}{10}$ and 10. This retains the functionality while allowing the DSP system to operate at a voltage 10 times lower than that dealt with by the current source and buffer/amplifiers. A voltage protection device is placed at the input to the DSP analog to digital converter. The only required high voltage components are now the buffer/amplifier and current source operational amplifiers. The resistor R_c sets the transconductance gain of the system. In order to minimize quantization error, a reasonable portion of the digital to analog converters range should be utilized. A larger resistor requires a larger voltage to provide a specified current. To maintain a unity transconductance, a gain equal to the value of the resistance R_c should be placed internally in the DSP algorithm or in series with a transfer function block diagram.

As discussed in Section 4.2.2, there are two approaches to designing the DSP algorithm. The first involves deriving the admittance transfer function of the network, then implementing the time domain response on the DSP. The second approach, using a graphical

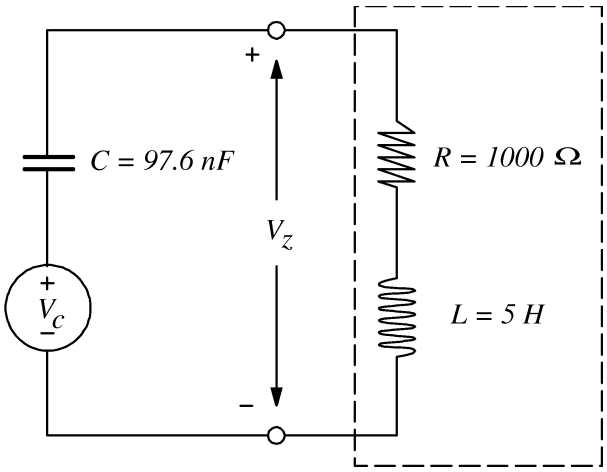

Figure 4.4: Ideal test circuit.

compilation package, does not require any derivations or coding and will be used here. The Real Time Workshop for MATLAB is now invoked to compile the Simulink[1] diagram into an executable code. This is downloaded onto the DSP hardware[2] and executed in real time. The sampling time of the digital system is 40 kHz. The current source and buffer/amplifiers required for the synthetic impedance are constructed from Burr-Brown OPA445 operational amplifiers. These operational amplifiers have a supply voltage limit of ± 45 v.

4.3.2 Test Example: Synthesizing a series $R - L$ impedance

Consider the circuit diagram shown in Figure 4.4. Suppose that it is desired to synthesize the L and R components, as for a single mode shunt. (Refer to Section 3.1.2 on page 31). The desired impedance is $Z_s = Ls + R$, thus $G(s) = Y(s) = \frac{1}{Ls+R}$, where $L = 5H$ and $R = 1000\Omega$. $Y(s)$ can be implemented using a digital signal processor. In this example, the dSpace[3] DSP system is used to simulate the required transfer function in real time (any other suitable DSP system may be used). The implementation of the voltage controlled current source is shown in Figure 4.5. To verify the correct operation, the frequency response was measured between the source voltage $V_c(s)$ and the synthetic impedance

[1] A graphical simulation environment for MATLAB.

[2] The target processing hardware is the dSpace DS1103 processing and I/O board.

[3] A real time DSP package for prototyping control systems.

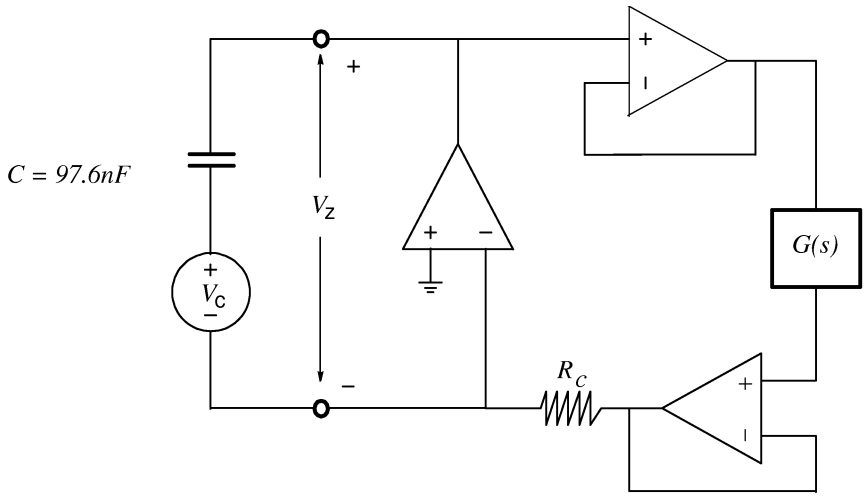

Figure 4.5: Test circuit with synthetic impedance.

$V_z(s)$. This is plotted along with the theoretical frequency response $|V_c(s)/V_z(s)|$ as shown in Figure 4.6. We can see that the simulated response along with the theoretical response in Figure 4.6 are closely matched, therefore verifying that the circuit developed agrees with expected results.

4.3.3 Shunt Damping Performance

The circuits of Figure(s) 3.2 is "redrawn" in Simulink as a transfer function block diagram using the methods described in Section 4.2.2. The resulting Simulink block diagrams are shown in Figure 4.7. The optimized series and parallel shunt elements from Section 3.4 are now applied to the simply supported beam. As shown in Section 4.3.1, the circuits are first converted into a transfer function block diagram, compiled with RTW, then downloaded onto the DSP hardware. The dSpace DS1103 processing and I/O board was chosen as the target DSP hardware

The displacement and voltage frequency responses are measured using a Polytec laser scanning vibrometer and a Hewlett Packard spectrum analyzer (35670A). In both cases a swept sine excitation is applied to the piezoelectric actuator. Figure 4.8 shows the theoretical and experimental damped frequency responses for both parallel and series multi-mode shunt circuits. Figure 4.9 shows the experimental time domain response, $V_{el}(0.170, s)/V_a(s)$, to a filtered step disturbance (band pass filtered between 40 and 200

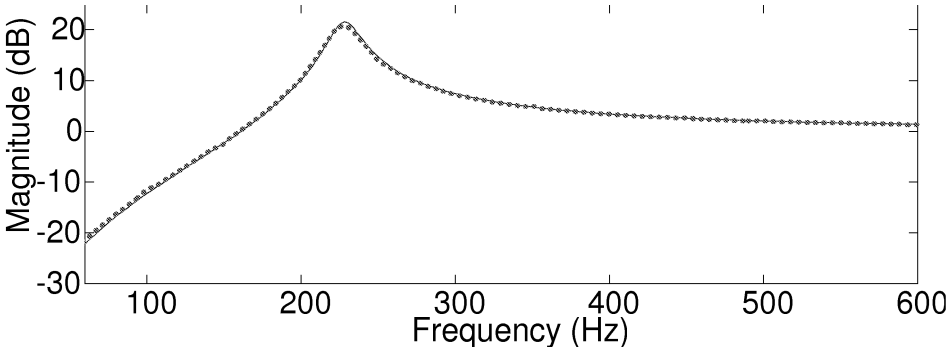

Figure 4.6: Theoretical (—) and experimental ($\cdots$) frequency responses, $|V_c(s)/V_z(s)|$.

Hz).

Experimental resonant amplitudes for the $2nd$ and $3rd$ modes were successfully reduced for both parallel and series cases using the synthetic impedance. Parallel resonant amplitudes were reduced by $19.8dB$ and 20.2 dB and in the series case a reduction of $20.3dB$ and $20.1dB$ was obtained.

4.4 Synthetic Impedance vs Direct Circuits

To evaluate the performance of the synthetic impedance, we need to compare it with the current *direct circuit* method (using discrete resistors, capacitors and virtual Riordan inductors [22]) and the predicated theoretical damped results. The performance was compared for both parallel and series multiple mode configurations, as shown in Figure 3.2, using the following parameters as outlined in Table 4.1.

The frequency response $|G_{yv}(0.170, s)|$, (obtained using the same procedure as described in Section 4.3.3), was plotted for both multiple mode shunt methods. The achieved experimental results are shown in Figures 4.10 and 4.11, for the $2nd$ and $3rd$ mode of the piezoelectric laminated simply supported beam. Note for Figures 4.10 and 4.11 that the following abbreviations represent: Exp. – experimental results, TM – theoretical model, SimZ – synthetic impedance and VC – virtual circuit.

Performance of the theoretical model (TM), synthetic impedance (SimZ) and virtual circuit (VC) results are shown in Table 4.2. From experimental results, the synthetic impedance closely agrees with the predicated theoretical results.

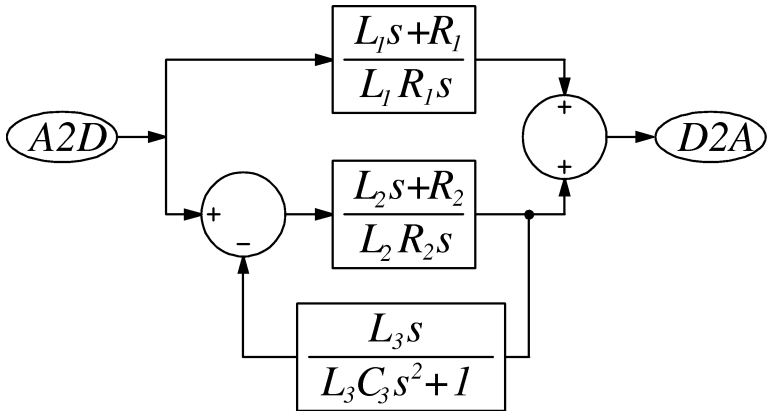

(a)

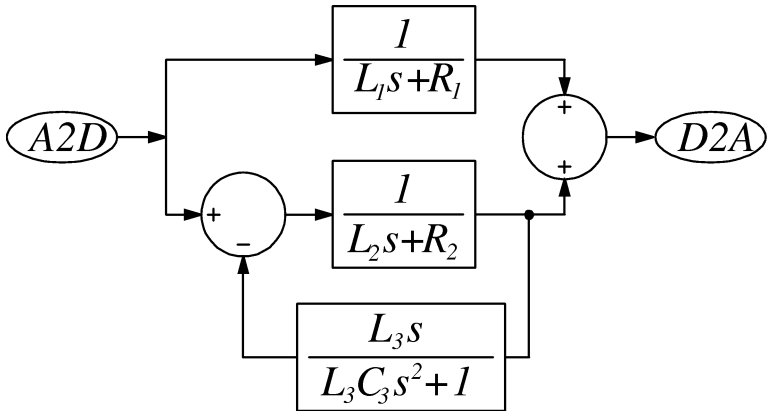

(b)

Figure 4.7: Admittance transfer function: (a) parallel and (b) series multi-mode shunts.

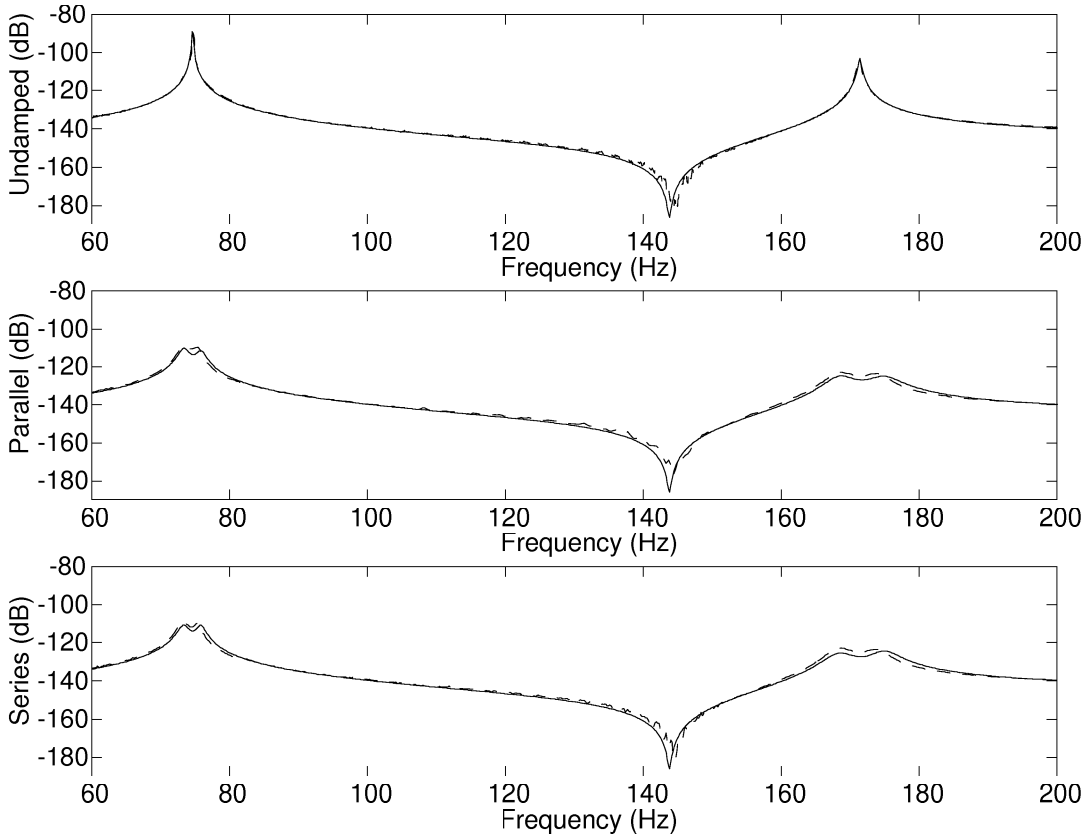

Figure 4.8: Parallel and series shunt circuit cases, $|G_{yv}(0.170, s)|$: experimental $(\cdots)$ and theoretical results (—).

Circuit Values		
	Parallel Case	Series Case
R_1^*	$262.75k\Omega$	1543.4Ω
R_2^*	$550.7k\Omega$	1145.2Ω
L_1	$43H$	$43H$
L_2	$20.9H$	$20.9H$
L_3	$45.2H$	$45.2H$
C_3	$100nF$	$100nF$

Table 4.1: Circuit values: theoretical model, virtual circuit and synthetic impedance.

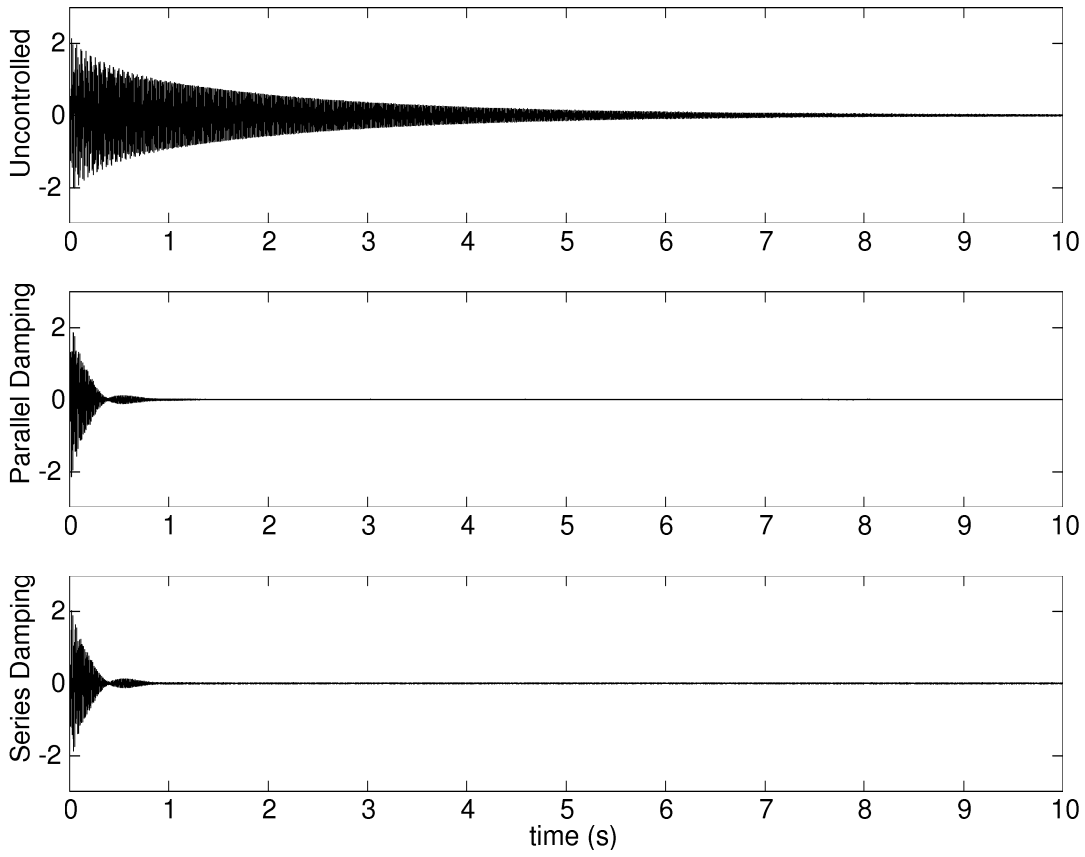

Figure 4.9: Experimental time domain results, $V_{el}(0.170, s)/V_a(s)$.

	Theoretical Model (TM)		**Synthetic Z (SimZ)**		**Virtual Circuit (VC)**	
Mode	Parallel	Series	Parallel	Series	Parallel	Series
$2nd$	$21.0dB$	$21.5dB$	$19.8dB$	$20.3dB$	$18.1dB$	$17.5dB$
$3rd$	$21.6dB$	$20.2dB$	$20.2\ dB$	$20.1dB$	$18.0dB$	$18.1dB$

Table 4.2: Compare amplitude reduction using benchmark circuit values: theoretical model, synthetic impedance and virtual circuit.

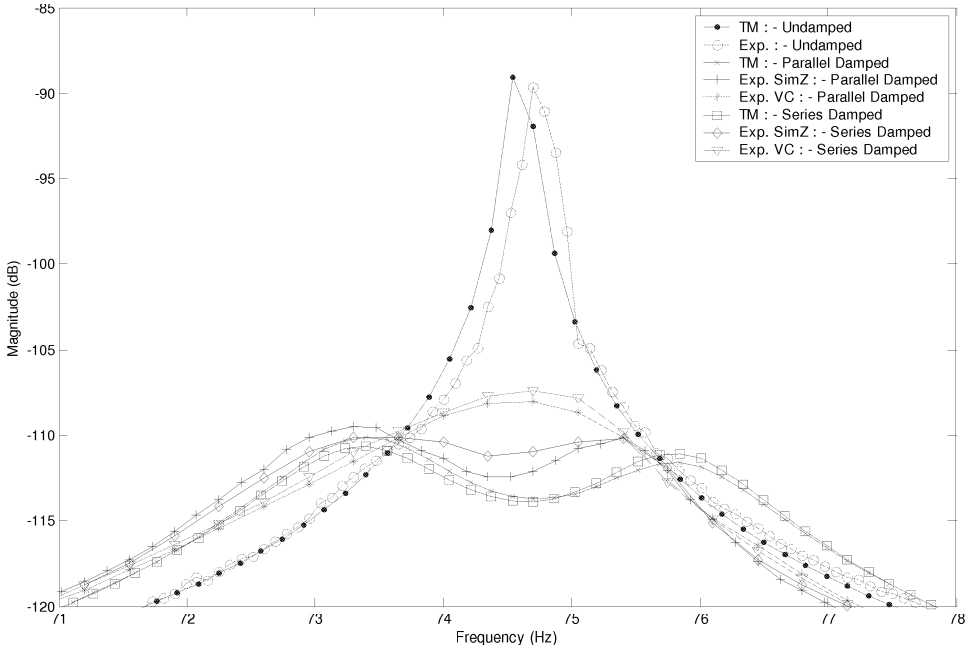

Figure 4.10: Compare 2*nd* mode theoretical model with experimental synthetic impedance and direct circuit results.

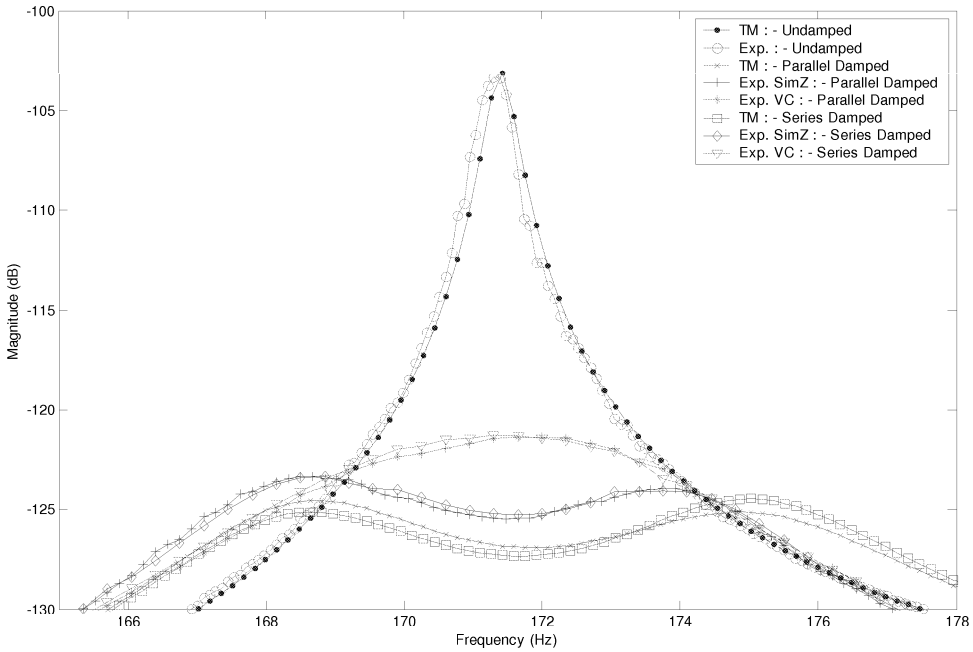

Figure 4.11: Compare 3*rd* mode theoretical model with experimental synthetic impedance and direct circuit results.

4.5 Chapter Conclusion

The problems associated with the *direct circuit* implementation mentioned in Section 4.1 have been addressed. Non-idealities in the virtual inductors result in a poor correlation between experimental and predicted frequency responses. Peak damping performance is $\approx 3dB$ lower than that achieved by the direct circuit method. The synthetic impedance has proven to be a high performance method of implementing shunt damping circuits. It has a low number of high voltage components, is immune to component non-ideality, and requires no tuning of sensitive virtual circuits. When using a DSP system, the synthetic impedance has the additional advantage that the shunt circuit parameters can be adjusted on-line, in real time.

Chapter 5

Shunt Damping using a Negative Capacitance Circuit

A passive vibration shunt damper generally acts to minimize structural vibration at a specific frequency associated with a lightly damped structural vibration mode. Because this frequency is rarely stationary in real applications, i.e. changes in climactic conditions may shift the resonant frequencies, some damping is usually added to ensure some level of effectiveness over a range of frequencies. Maximum amplitude reduction, however, is achieved only if the shunt absorber is lightly damped and accurately tuned to the required frequency of concern. Thus, a semi-active (passive-active) vibration absorber should perform better than a passive shunt and, furthermore, could be made much simpler.

5.1 Introduction

There are many different types of semi-active vibration controller schemes. One of the many semi-active vibration schemes involves modifying the effective stiffness of the piezoelectric element, such as switch damping [4, 6, 7, 20, 21]. Switch damping involves switching the piezoelectric actuator element between high (open-circuit) and low (short-circuit) stiffness states. These techniques are broadband and passive, but the amplitude reduction performance is limited.

Another type of semi-active vibration controller is the active-passive hybrid piezoelectric network (APPN), which involves using a passive shunt damping technique in conjugation with an appropriate broadband active controller (e.g. a simple $R-L$ passive shunt with a

LQG active controller). This method is claimed to be more effective than a system with separated active and passive control schemes [1, 3, 23, 24].

This chapter will attempt to developed a new technique for semi-active (passive-active) control. The "negative capacitor" controller is studied theoretically and then validated experimentally. The negative capacitor controller is similar in nature to passive shunt damping techniques; a single piezoelectric transducer is used, but is capable of damping multiple modes. In order to present the new semi-active shunt dampener, the composite system dynamics need to be considered.

5.2 Modeling the Composite System in Transfer Function Form

The transfer function between the displacement at any point along the beam and the actuator voltage $G_{yv}(x,s)$, and between the shunting piezoelectric voltage and the actuator voltage $G_{vv}(s)$, were found in Section 2.3 as

$$G_{yv}(x,s) \triangleq \frac{Y(x,s)}{V_a(s)} = \sum_{i=1}^{\infty} \frac{C_a[\phi_i'(x_1) - \phi_i'(x_2)]\phi_i(x)}{s^2 + 2\zeta_i\omega_i s + \omega_i^2} \tag{5.1}$$

and

$$G_{vv}(s) \triangleq \frac{V_s(s)}{V_a(s)} = \sum_{i=1}^{\infty} \frac{C_s C_a[\phi_i'(x_1) - \phi_i'(x_2)][\phi_i'(x_3) - \phi_i'(x_4)]}{s^2 + 2\zeta_i\omega_i s + \omega_i^2}. \tag{5.2}$$

With reference to Figure 5.1, we can also derive the following transfer functions if a disturbance signal $F(r,s)$ at $x = r$ is applied to the beam structure, e.g. a point force disturbance, as [18]

$$G_{vf}(s) \triangleq \frac{V_s(s)}{F(r,s)} = \sum_{i=1}^{\infty} \frac{C_s[\phi_i'(x_4) - \phi_i'(x_3)]\phi_i(r)}{s^2 + 2\zeta_i\omega_i s + \omega_i^2} \tag{5.3}$$

and

$$G_{yf}(x,s) \triangleq \frac{Y(x,s)}{F(r,s)} = \sum_{i=1}^{\infty} \frac{\phi_i(x)\phi_i(r)}{s^2 + 2\zeta_i\omega_i s + \omega_i^2}. \tag{5.4}$$

When modeling the piezoelectric element, there are two different models, as shown in Figure 1.1. Both concepts are presented in papers [8, 9, 13, 26]. The most common of these piezoelectric models considers the piezoelectric element as a capacitor C_p in series with a voltage source $V_p(s)$, which is dependent on the dynamics of the resonant structure

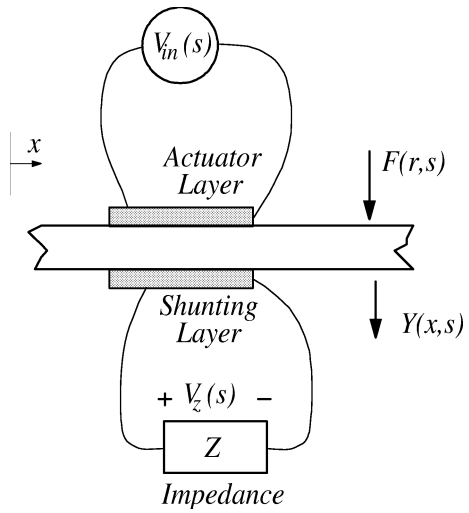

Figure 5.1: Flexible structure with piezoelectric patches attached.

[13]. This chapter will only consider the series piezoelectric model, as in Figure 1.1 (b), but can be extended for the parallel case, as in Figure 1.1 (a).

Consider Figures 5.2, where a piezoelectric patch is shunted by an impedance Z. Hence, the current-voltage relation of the impedance can be represented in Laplace domain as

$$V_z(s) = I_z(s)Z(s), \tag{5.5}$$

where V_z is the voltage across the impedance and I_z is the current flowing through the impedance Z. Using Kirchhoff's voltage law in the circuit shown in Figure 5.2, we obtain the following relationship $V_z(s)$ as

$$V_z(s) = V_p(s) - \frac{1}{C_p s} I_z(s), \tag{5.6}$$

where V_p is the voltage induced from the electromechanical coupling effect [13] and C_p represents capacitance of the shunting layer. Using (5.5) and (5.6) we obtain

$$V_z(s) = \frac{Z(s)}{\frac{1}{C_p s} + Z(s)} V_p(s) \tag{5.7}$$

or

$$V_z(s) = \frac{C_p s Z(s)}{1 + C_p s Z(s)} V_p(s).$$

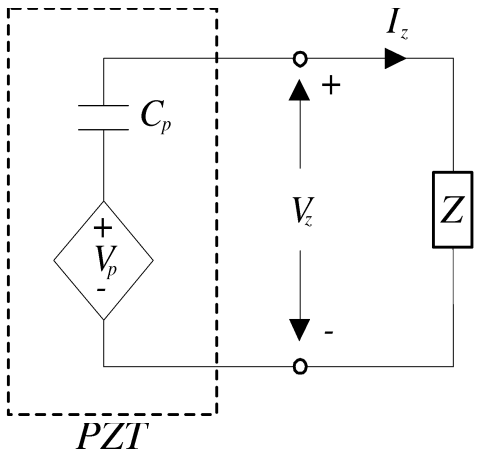

Figure 5.2: Schematic of piezoelectric shunting layer with a shunting impedance Z present.

Notice that when $Z = \infty$, i.e. for an open-circuit, we have

$$Z = \infty \quad \Rightarrow \quad V_z(s) \triangleq V_p(s) = G_{vv}(s)V_{in}(s). \tag{5.8}$$

However, if the circuit is shunted by Z, we can assume that

$$V_p(s) = G_{vv}(s)V_{in}(s) - G_{vv}(s)V_z(s) \quad s.t \quad Z \neq \infty, 0. \tag{5.9}$$

Note: These essential equations (5.8) and (5.9) are reported in state-space form in reference [11], as the *sensing* and *actuator equations*, where (5.8) is part of *sensing equation* and (5.9) is the *actuator equation.*

By substituting (5.7) into the above equation, $V_p(s)$ is found to be

$$V_p(s) = G_{vv}(s)V_{in}(s) - G_{vv}(s)\frac{Z(s)}{\frac{1}{C_p s} + Z(s)}V_p(s).$$

Using simple algebra, the transfer function relating $V_p(s)$ to $V_{in}(s)$ can be found as

$$\frac{V_p(s)}{V_{in}(s)} = \frac{G_{vv}(s)}{1 + G_{vv}(s)K(s)}, \tag{5.10}$$

where

$$K(s) = \frac{Z(s)}{Z(s) + \frac{1}{C_p s}}. \tag{5.11}$$

Note that if $V_p(s)$ is dynamically equivalent to $V_s(s)$, then the following relationships hold:

$$\hat{G}_{vv}(s) \triangleq \frac{V_s(s)}{V_{in}(s)} = \frac{G_{vv}(s)}{1 + G_{vv}(s)K(s)} \tag{5.12}$$

and

$$\hat{G}_{yv}(x,s) \triangleq \frac{Y(x,s)}{V_{in}(s)} = \frac{G_{yv}(s)}{1 + G_{vv}(s)K(s)}. \tag{5.13}$$

We can see from the above equations (5.12) and (5.13) that shunt damping is a simple negative-feedback control problem. Therefore, the classical control theory can be applied to gain a better understanding of the compound system.

Aside, from reference [18], the actuator voltage $V_a(s)$ is given by:

$$V_a(s) = V_{in}(s) - K(s)V_s(s). \tag{5.14}$$

We can define the transfer functions shown in Figure 5.3 as follows:

$$G_{vf}(s) \triangleq \tfrac{V_s(s)}{F(r,s)} \quad G_{vv}(s) \triangleq \tfrac{V_s(s)}{V_a(s)}$$

$$G_{yf}(x,s) \triangleq \tfrac{Y(x,s)}{F(r,s)} \quad G_{yv}(x,s) \triangleq \tfrac{Y(x,s)}{V_a(s)}.$$

With the above definitions, the sensor shunt voltage is given by:

$$V_s(s) = G_{vf}F(r,s) + G_{vv}(s)V_a(s). \tag{5.15}$$

After substituting (5.14) in the above expression, $V_s(s)$ becomes

$$V_s(s) = G_{vf}F(r,s) - G_{vv}(s)K(s)V_s(s) + G_{vv}(s)V_{in}(s). \tag{5.16}$$

On rearranging, the sensor voltage in terms $V_s(s)$ is

$$V_s(s) = \frac{G_{vf}(s)F(r,s)}{1 + K(s)G_{vv}(s)} + \frac{G_{vv}(s)V_{in}(s)}{1 + K(s)G_{vv}(s)} \tag{5.17}$$

and the displacement $Y(x,s)$ at a given location x is

$$Y(x,s) = \frac{G_{yf}(s)F(r,s)}{1 + K(s)G_{vv}(s)} + \frac{G_{yv}(s)V_{in}(s)}{1 + K(s)G_{vv}(s)}. \tag{5.18}$$

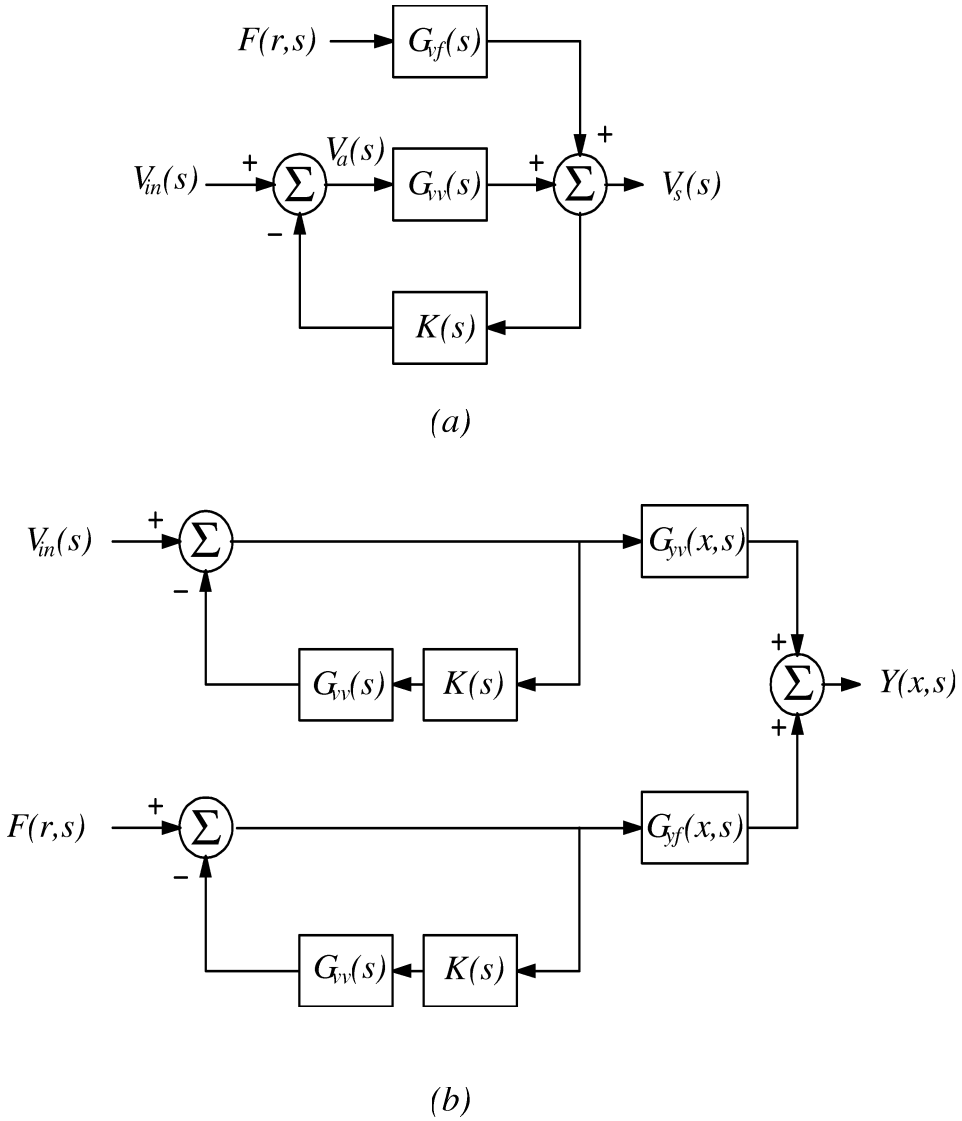

Figure 5.3: Composite system transfer function block diagram.

5.3 Developing the Negative Capacitance Controller

This section will develop the fundamental concept of the new broadband semi-active controller. Consider the two following relationships, as in Section 5.2,

$$\hat{G}_{vv}(s) = \frac{G_{vv}(s)}{1 + G_{vv}(s)K(s)} \tag{5.19}$$

and

$$K(s) = \frac{Z(s)}{Z(s) + \frac{1}{C_p s}}, \tag{5.20}$$

where $G_{vv}(s)$ is the undamped response of the structure, C_p is the piezoelectric capacitance, and $Z(s)$ is the impedance of the shunt network. By substituting (5.19) and (5.20) we obtain the following relationship for $\hat{G}_{vv}(s)$, i.e. the transfer function of a shunt damped mechanical structure as

$$\hat{G}_{vv}(s) = \frac{G_{vv}(s)\left(C_p Z(s)s + 1\right)}{C_p Z(s)s\left(1 + G_{vv}(s)\right) + 1}. \tag{5.21}$$

The damped structural transfer function (5.21) can be minimized by equating the numerator to 0, i.e. by selecting $Z(s) = \frac{1}{-Cs}$, where $C = C_p$. This is not a realizable network as it creates an undamped electrical resonance. A compromise between damping performance and practicality (i.e. the node voltages and currents) can be achieved by introducing a series resistor R. The electrical model of the shunt piezoelectric with attached negative capacitor and resistor is shown in Figure 5.4. It should be noted that this control scheme is virtually immune to variations in structural dynamics since it is not tuned into specific frequencies, unlike passive shunt damping.

If $Z(s)$ is chosen to be $-\frac{1}{Cs} + R$, then $Z(s)$ will have the following transfer function:

$$Z(s) = \frac{RCs - 1}{Cs}. \tag{5.22}$$

Substituting (5.22) in (5.20), $K(s)$ becomes

$$K(s) = \frac{s - \frac{1}{RC}}{s + \frac{1}{RC}\left(\frac{C}{C_p} - 1\right)}. \tag{5.23}$$

The shunt damped system will be stable if the capacitance of the controller $K(s)$ is greater than or equal to the capacitance of the piezoelectric patch, i.e. if $C \geq C_p$ [2]. In practice, the equivalent electrical model of the piezoelectric element does not fully describe the

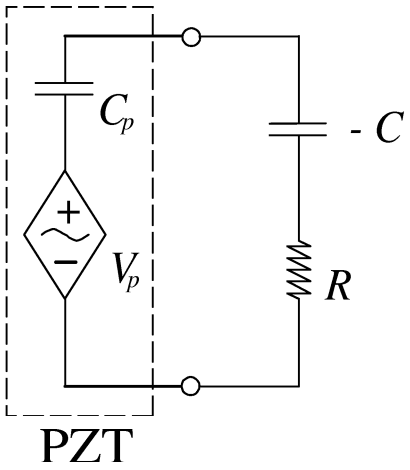

Figure 5.4: Negative capacitance controller with appropriate damping resistance.

piezoelectric dynamics, in particular the piezoelectric capacitance tends to be frequency dependent. To deal with this uncertainty, C is chosen conservatively, i.e. $C > C_p(f)$ $\forall f \in \mathbb{R}$. For our case, C was chosen to be $115nF$, since $C_p = 105nF$.

In summary, we want to cancel out the capacitance of the piezoelectric element C_p and dissipate the electrical energy of the system via a resistor R. We will see that it is important to select an appropriate resistive value that maximizes the damping of the structure for a range of structural modes, say 5 modes.

5.4 Optimal R Damping using $\mathcal{H}_2$ norm Optimization

In order to find the appropriate value for resistor R, an optimization approach is proposed, such that the $\mathcal{H}_2$ norm of the combined system is minimized for 5 structural modes. From Section 3.3.1, we have the following optimization problem:

$$R^* = \arg \min_{\substack{s.t.\ \hat{\mathbf{A}}(R)^T\hat{\mathbf{P}}+\hat{\mathbf{P}}\hat{\mathbf{A}}(R)+\hat{\mathbf{B}}\hat{\mathbf{B}}^T=\mathbf{0} \\ R>0}} tr(\hat{\mathbf{C}}\hat{\mathbf{P}}\hat{\mathbf{C}}^T) \quad , \tag{5.24}$$

where $\hat{G}_{yv}(0.170, s) = \hat{\mathbf{C}}(s\mathbf{I} - \hat{\mathbf{A}}(R))^{-1}\hat{\mathbf{B}}$. Note that $\hat{\mathbf{A}}$ is a function of R. For optimality we take the derivatives of L, with respect to parameters $\hat{\mathbf{P}}$, $\hat{\mathbf{S}}$ and R, and set the derivatives to zero, such as

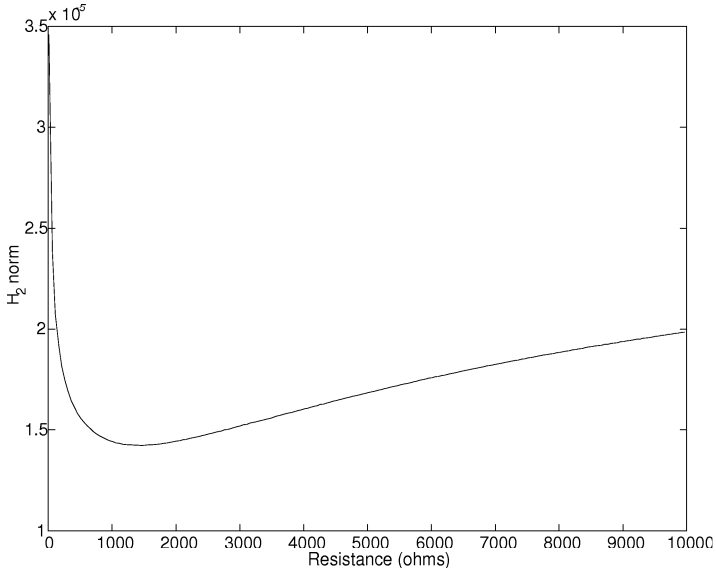

Figure 5.5: $G_{yv}(0.170, s)$ $\mathcal{H}_2$ norm plotted against resistance R (Ω), for 5 modes.

$$\frac{\partial L}{\partial \hat{\mathbf{S}}} = \hat{\mathbf{A}}(R)\hat{\mathbf{P}} + \hat{\mathbf{P}}\hat{\mathbf{A}}(R)^T + \hat{\mathbf{B}}\hat{\mathbf{B}}^T = \mathbf{0} \tag{5.25}$$

$$\frac{\partial L}{\partial \hat{\mathbf{P}}} = \hat{\mathbf{A}}(R)^T\hat{\mathbf{S}} + \hat{\mathbf{S}}\hat{\mathbf{A}}(R) + \hat{\mathbf{C}}^T\hat{\mathbf{C}} = \mathbf{0} \tag{5.26}$$

$$\frac{\partial L}{\partial R} = tr\left(\hat{\mathbf{E}}\hat{\mathbf{P}}\hat{\mathbf{S}} + \hat{\mathbf{P}}\hat{\mathbf{E}}^T\hat{\mathbf{S}}\right) = 0, \tag{5.27}$$

where $\hat{\mathbf{A}} = \bar{\mathbf{A}} + R\hat{\mathbf{E}}$ and matrix $\bar{\mathbf{A}}$ is not a function of R.

Using the same numerical approach as in Section 3.3.1, the optimization algorithm found a local minimum at $R^* = 1309.9\Omega$. Figure 5.5 shows the $\mathcal{H}_2$ norm cost surface which contains a minima at R^*.

5.5 Simulated Results

Using $C = 115nF$ and $R^* = 1309.9\Omega$, simulations of $G_{yv}(0.170, s)$ and $\hat{G}_{yv}(0.170, s)$ show that the structural modes of the structure have been considerably dampened, as shown in Figure 5.6. From Figure 5.7, we can see that the poles of the compound system have moved to the left of the imaginary axis. By shifting the poles to the left, we have added damping

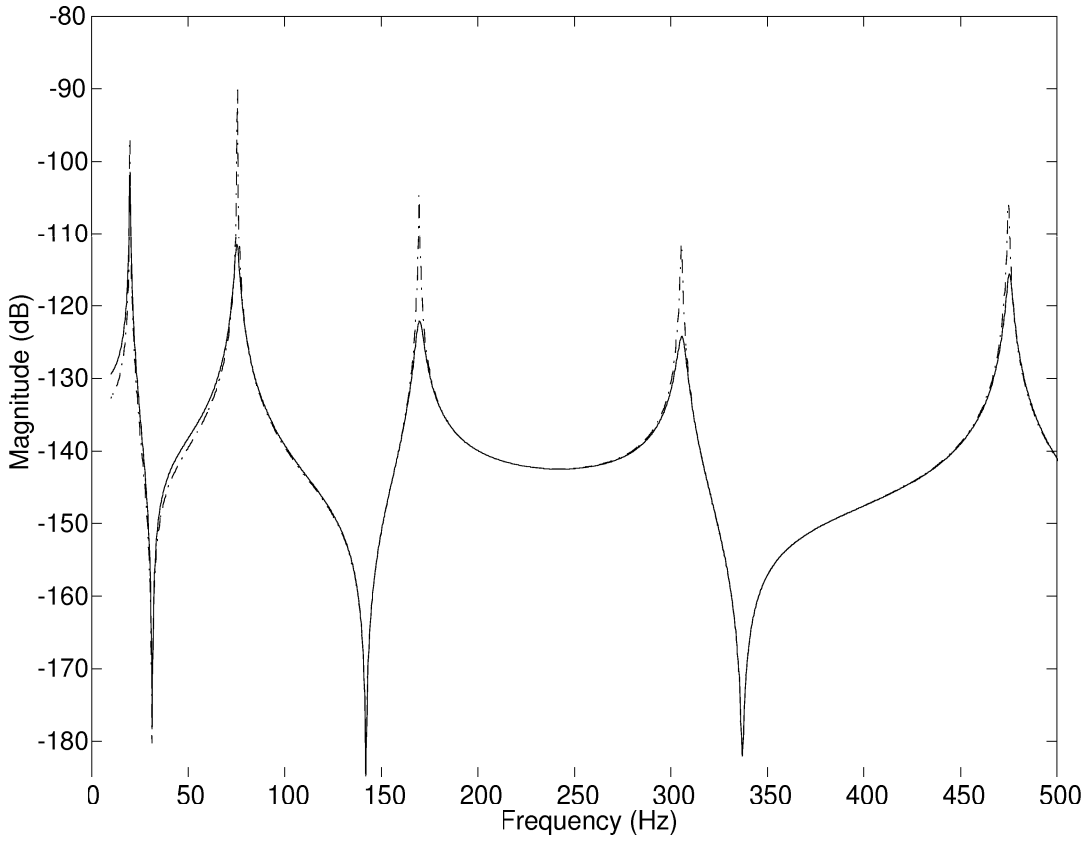

Figure 5.6: Simulated responses: $|G_{yv}(0.170, s)|$ undamped $(\cdots)$ and $\left|\hat{G}_{yv}(0.170, s)\right|$ damped system (—).

to the compound system, therefore effectively minimizing vibration of the structure. From Figure 5.7, we can foresee that the controller has a localized effect on the close-loop poles.

5.6 Experimental Results

5.6.1 Creating the Negative Capacitance

If our semi-active shunt circuit requires a negative capacitance element, how do we create such an element? To answer this question we begin with the following circuit given in Figure 5.8. If we use nodal analysis, at node 1 the Kirchhoff's current law implies

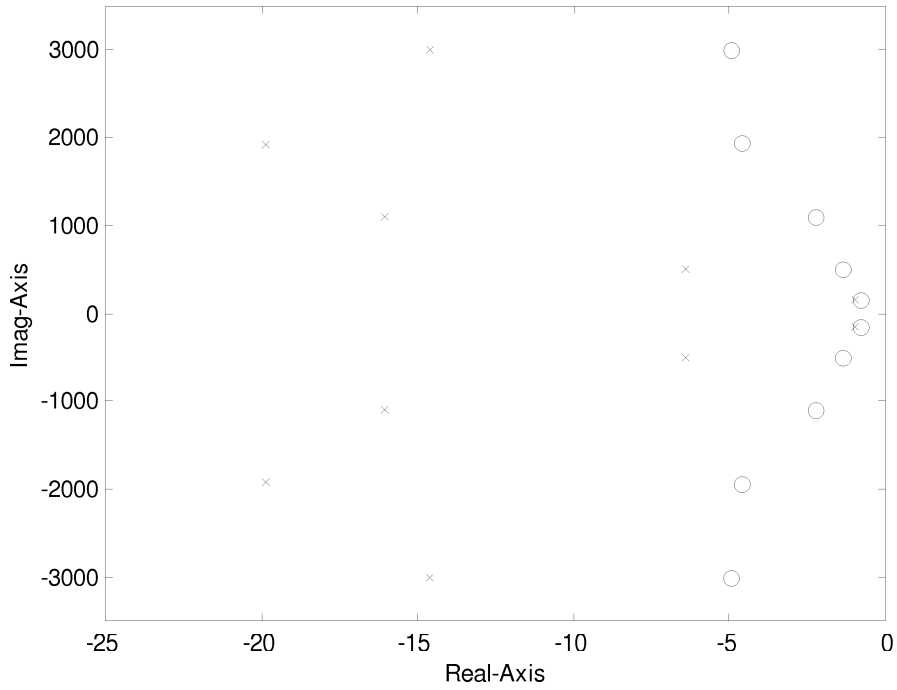

Figure 5.7: $G_{yv}(0.170, s)$ undamped poles (o) and $\hat{G}_{yv}(0.170, s)$ damped poles ($\times$).

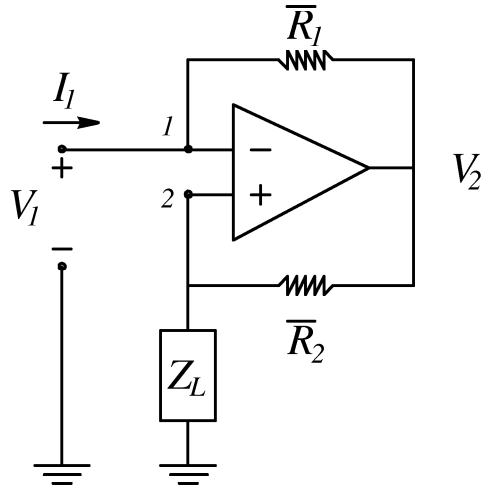

Figure 5.8: Example of a negative impedance converter.

$$I_1 + \frac{V_2 - V_1}{\bar{R}_1} = 0 \tag{5.28}$$

and at node 2,

$$\frac{V_2 - V_1}{\bar{R}_2} + \frac{(0 - V_1)}{Z_L} = 0. \tag{5.29}$$

Eliminating V_2 from the two equations (5.28) and (5.29) gives us

$$-I_1\bar{R}_1 - \frac{V_1\bar{R}_2}{Z_L} = 0. \tag{5.30}$$

Solving for the ratio $\frac{I_1}{V_1}$, we obtain the following

$$Z_{in} = \frac{V_1}{I_1} = -\frac{\bar{R}_1}{\bar{R}_2}Z_L \tag{5.31}$$

or alternatively, $Y_{in} = -\bar{R}_2/\bar{R}_1 Y_L$.

From these equations we can see that the circuit, shown in Figure 5.8, creates a negative impedance and also scales the value by the ratios of the resistors, i.e. a transconductance gain. Thus if $Z_L = 1/Cs$, then $Z_{in} = -1/Cs$. The circuit shown is one of a general class of circuits known as a *negative impedance converter* (NIC).

We can now use this circuit for reducing the amplitudes of the resonant peaks of the structure. When considering this type of circuit, we need to be aware that the impedance Z has become a semi-active shunt circuit. Therefore, stability issues need to be addressed when constructing the experimental circuit.

5.6.2 Test Example: Negative Capacitance

A test circuit was constructed, as in Figure 5.9, with the appropriate components, as outlined in Table 5.1. Construction of the test circuit incorporated Burr-Brown OPA445 high voltage operational amplifiers. The frequency response was measured between the source voltage $\tilde{V}_{in}$, and the voltage across the semi-active controller $\tilde{V}_{out}$ as shown in Figure 5.9. The simulated magnitude and phase response are plotted against the experimental responses, as illustrated in Figure 5.10. From experimental results we can see that the predicted theoretical results agree closely, therefore verifying that the semi-active shunt controller is working correctly.

Circuit Component	Value
$\bar{R}$	$10k\Omega$
$\underline{R}$	$33M\Omega$
$\bar{C} \approx C_p$	$100nF$
C	$115nF$
R	$1.3k\Omega$

Table 5.1: Parameters of negative capacitance test circuit.

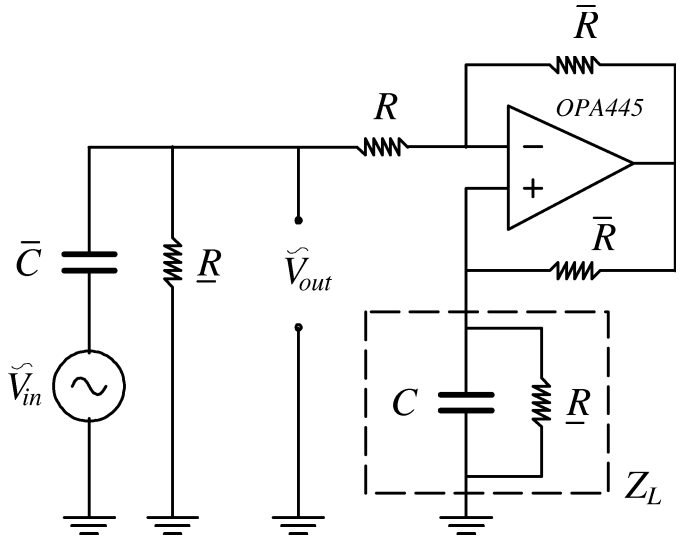

Figure 5.9: Test circuit with negative capacitance present.

5.6.3 Semi-active Shunt Damping

Using the tested circuit from above, the semi-active controller is now applied to the piezoelectric laminated simply supported beam. The displacement and actuator voltage frequency responses are measured using a Polytec laser scanning vibrometer (PSV-300) and the Hewlett Packard function generator (33120A). A swept sine excitation is amplified then applied to the piezoelectric actuator.

The experimental resonant amplitudes for the $1st$, $2nd$, $3rd$, $4th$ and $5th$ modes were successfully reduced as shown in Figure 5.11. Resonant amplitudes were reduced by 6.1, 16.3, 15.2, 11.7 and $10.2dB$ respectively. From theoretical simulations, the resonant ampli-

Negative Capacitance Amplitude Reduction		
Mode	Theoretical Simulations (dB)	Experimental (dB)
1	7.3	6.1
2	22.4	16.3
3	18.6	15.2
4	13.4	11.7
5	11.8	10.2

Table 5.2: Amplitude reduction: simulations and experimental results.

tudes $1st$, $2nd$, $3rd$, $4th$ and $5th$ modes were 7.3, 22.4, 18.6, 13.4 and 11.8dB respectively. The analytical and experimental results show encouraging developments, as summarized in Table 5.2.

5.7 Chapter Conclusion

This chapter has introduced a new type of semi-active (passive-active) controller. The "negative capacitor" piezoelectric shunt circuit has been introduced as an alternate method of reducing structural vibrations. The negative capacitor has a number of advantages over current passive shunt damping systems: simplicity, robustness and broadband disturbance attenuation.

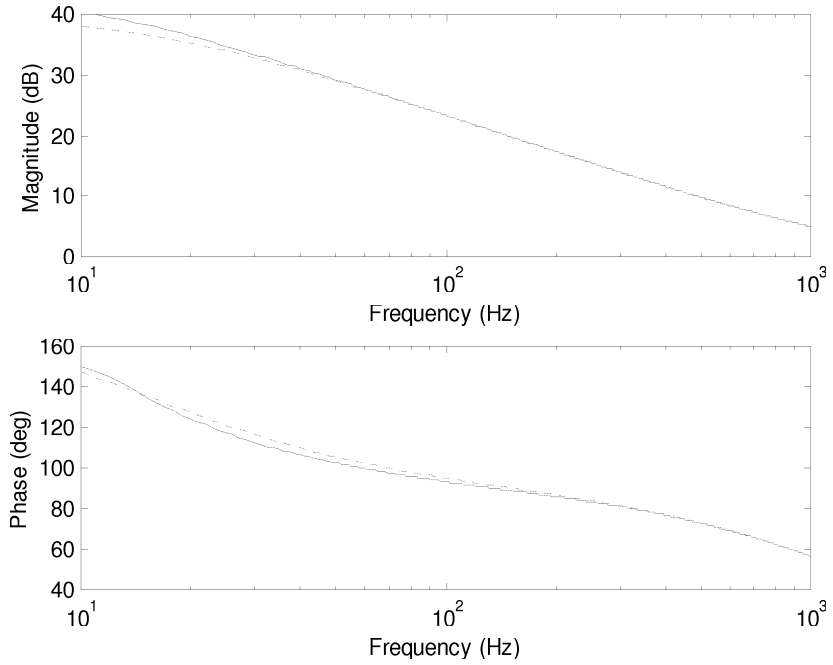

Figure 5.10: Frequency responses $\tilde{V}_{out}(s)/\tilde{V}_{in}(s)$ of the test circuit: ideal $(\cdots)$ and experimental results (—).

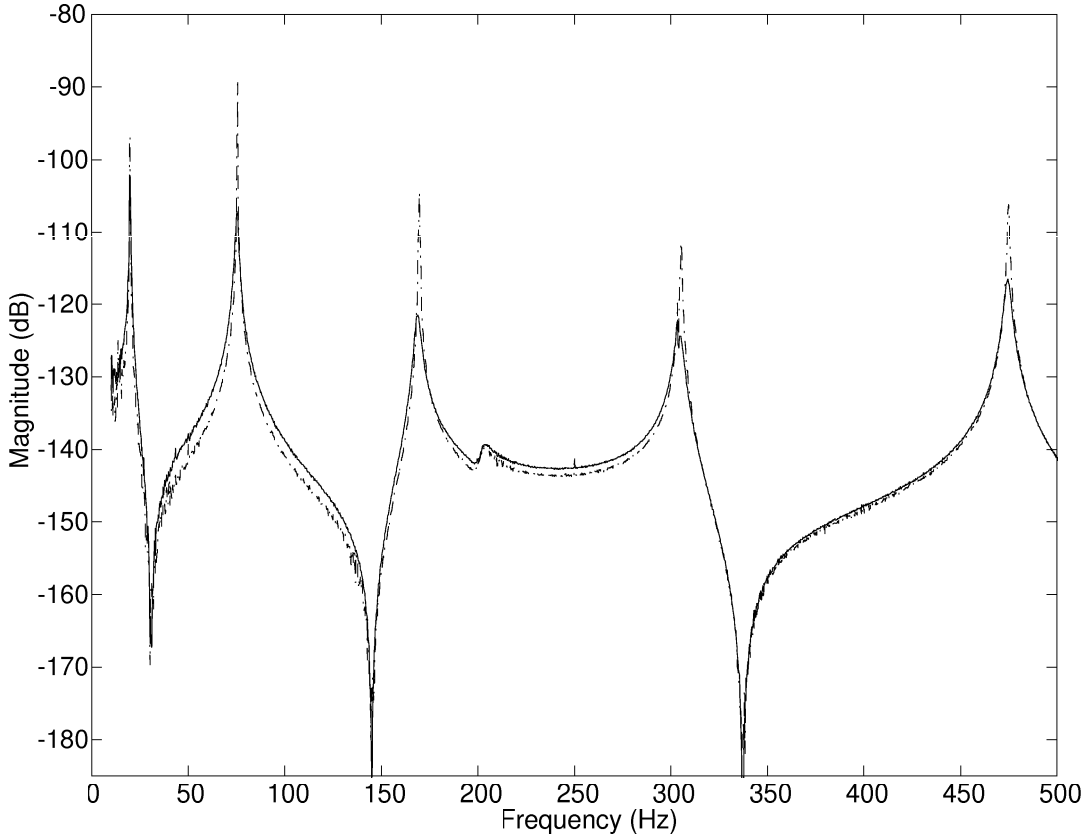

Figure 5.11: Experimental responses: $|G_{yv}(0.170, s)|$ undamped $(\cdots)$ and $\left|\hat{G}_{yv}(0.170, s)\right|$ damped system (—).

Chapter 6

Conclusions and Further Research

6.1 Conclusion

6.1.1 Physical Modeling

From this chapter we developed a comprehensive understanding of how to model a simple resonant structure using the Euler-Bernoulli beam equation and modal analysis. Experimental results match theoretical modeling of the piezoelectric laminated simply supported beam.

6.1.2 Passive Shunt Damping

An optimization based method for obtaining the optimal resistances for multi-mode shunt damping was presented. The method is intended to solve the difficulties encountered in previous multi-mode damping [28, 29]. By using this technique, it is possible to determine the required resistances and/or a starting point for fine-tuning of the shunt circuits in a systematic manner. The optimization technique provides an easy and reliable way of obtaining the optimal resistance for multi-mode damping. It also eliminates the tedious trial and error method of obtaining the optimal shunt resistance [9, 12, 14, 27, 28, 29, 30].

From the $\mathcal{H}_2$ cost surfaces, it can be inferred that the parallel shunt circuit case is less sensitive to resistance tuning than the series circuit case and this is due to the relative flatness of the cost function in the vicinity of a minimum. This justifies the experimental work presented in [27], that the *"parallel case is more practical for circuit tuning"*.

In the experiments, two multi-mode shunt circuits, namely the parallel and series shunts,

of a piezoelectric laminated simply supported beam were implemented. The experimental results were very encouraging. Even though only two modes were shunted, the optimization technique can be extended to incorporate more modes.

A distinct characteristic of this technique is that it can be easily extended to the case when several piezoelectric patches are to be shunt damped on the same resonant structure.

6.1.3 Synthetic Impedance

Previous shunt damping methodologies have also suffered from issues relating to the difficulty in implementing the passive shunt network. A synthetic impedance has been presented that implements the terminal impedance of a specified shunt network. The synthetic impedance also provides a means for designing circuit network substitutes with arbitrary response and functionality. The concepts presented have been experimentally verified with good results. The modal resonant magnitudes have been reduced by up to $20dB$; this corresponds to a damped settling time $\frac{1}{10}^{\text{th}}$ that of the free response[1]. In general, theoretical predictions have been coherent with experimental results.

6.1.4 Shunt Damping using a Negative Capacitance Circuit

The negative capacitor piezoelectric shunt circuit has been introduced as an alternate method of reducing structural vibrations. While achieving comparable performance, the negative capacitor has a number of advantages over current passive shunt damping systems: simplicity - it is non-model based and requires only a single operational amplifier for implementation; and robustness - the negative capacitor depends only on the dynamics of the piezoceramic device. A method has been presented for synthesizing a semi-active controller that alleviates some of the problems associated with active and passive control schemes with promising results. Resonant magnitudes have been reduced up to $16dB$ for multiple modes.

[1] For the excitation described in Section 4.3.3.

6.2 Suggestions for Further Research

6.2.1 Active Shunt Controllers

Future work could involve remodeling the passive shunt damping problem in an active feedback control systems perspective. Since we know the relation $\frac{I_z(s)}{V_z(s)} = \frac{1}{Z(s)} = G_z(s)$, where $V_z(s)$ is the voltage being sensed by the synthetic impedance and $I_z(s)$ is the current produced by the synthetic impedance, we can apply different active controller strategies to determine $G_z(s)$, such as LQG and $\mathcal{H}_\infty$ optimal control strategies. This is now possible, as an impedance of arbitrary structure can be implemented using the synthetic impedance.

6.2.2 Negative Capacitance (Semi-active Controller)

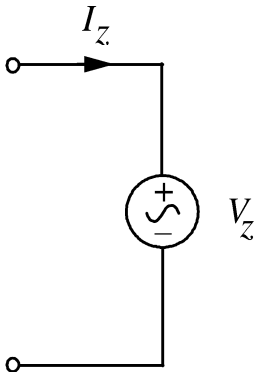

Figure 6.1: Current controlled voltage sources.

A number of future issues need to be addressed for the semi-active controller. These are:

1. To understand and model the structural uncertainty associated with the piezoelectric element, we need to consider the frequency dynamics of the piezoelectric shunt.

2. To develop an impedance Z, such that it senses a current I_z and outputs a voltage V_z, as shown in Figure 6.1, similar to the synthetic impedance as derived in Section 6.1, but as a current controlled voltage source. This type of impedance can be used to simulate the required semi-active controller, i.e. $Z(s) = \frac{CRs-1}{Cs}$.

Appendix A

Summary of Active Inductors

A.1 Grounded Simulated Inductor

To simulate large inductance values, say $1H$ to $15,000H$, we need to use active elements, i.e. operational amplifiers. The most successful is the Riordan's grounded gyrator [22]. It is claimed that these gyrators have the lowest sensitivity to component variations. This circuit is shown in Figure A.1 and is seen to consist of two operational amplifiers and five impedances. To analyze this circuit, using the appropriate nodal analysis, we observe that

$$V_2 = V_1\left(1 + \frac{Z_4}{Z_5}\right)$$

and that

$$V_3 = V_1\left(1 + \frac{Z_2}{Z_3}\right) - V_2\left(\frac{Z_2}{Z_3}\right)$$

or

$$V_3 = V_1\left(1 + \frac{Z_2 Z_4}{Z_3 Z_5}\right).$$

Now the input current is

$$I_1 = \frac{V_1 - V_3}{Z_1} = V_1\frac{Z_2 Z_4}{Z_1 Z_3 Z_5}.$$

Thus, the input impedance is seen to be

$$Z_{in} = \frac{V_1}{I_1} = \frac{Z_1 Z_3 Z_5}{Z_2 Z_4}. \tag{A.1}$$

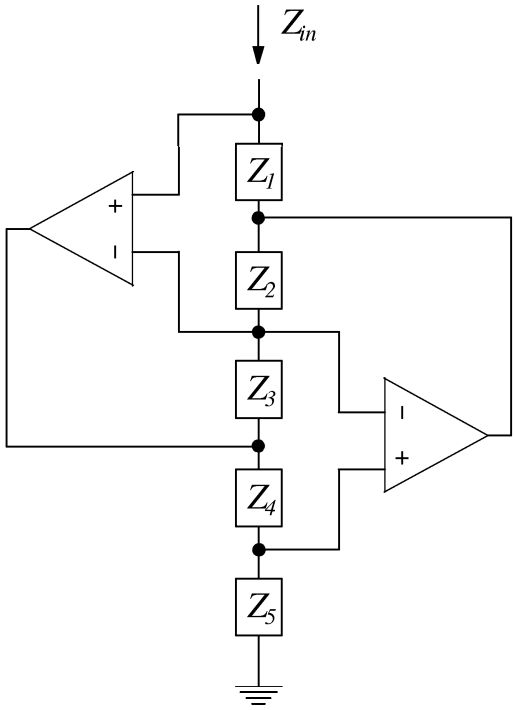

Figure A.1: Simulated grounded inductor.

From this equation we see that if either Z_2 or Z_4 are capacitors, such that $Z = \frac{1}{Cs}$ and all remaining elements are resistors of value R, then the last equation becomes

$$Z_{in} = \left(CR^2\right) s = L_{eq} s \tag{A.2}$$

and the circuit behaves as if it were an inductor of value

$$L_{eq} = CR^2. \tag{A.3}$$

For example, if $C = 0.01\mu F$ and four resistors have the value $R = 1k\Omega$, then at the input, the circuit appears to be a $10mH$ inductor.

A.2 Floating Simulated Inductor

One problem with gyrator circuits has been the difficulty of making "floating" inductors: - both terminals are accessible. It is possible to make a *floating* inductor with two gyrator

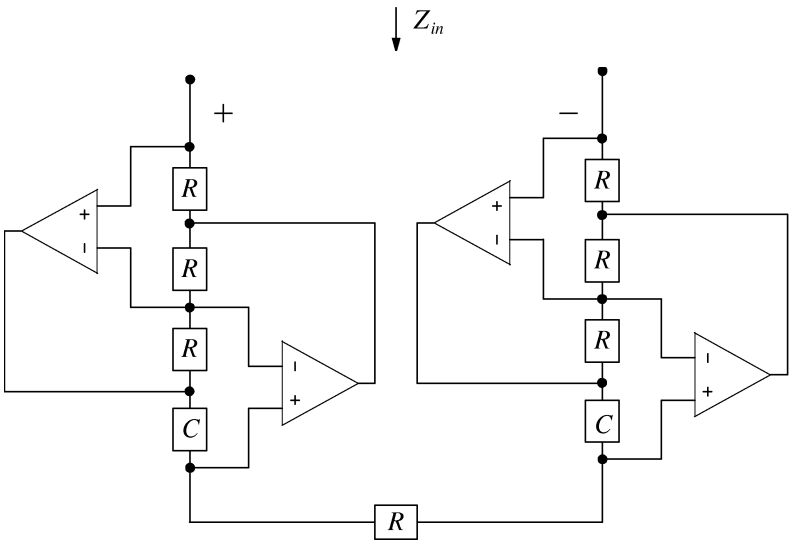

Figure A.2: Simulated floating inductor.

circuits and this usually requires four operational amplifiers. The realization of a *floating* inductor is to connect two identical grounded inductors back-to-back as shown in Figure A.2. It is straightforward to show that the input impedance is

$$Z_{in} = \left(CR^2\right) s = L_{eq} s. \tag{A.4}$$

Riordan [22] presented the floating inductor in his early papers. The floating element of our present interest is the floating inductor for which the two terminals may be at different voltages, neither equal to zero (or grounded). A representation of such an inductor is shown in Figure A.2 where the two terminals are floating. With a floating inductor all the elements must be matched, i.e. all resistance and capacitance must have the same values.

Appendix B

Beam Parameters

Length, L	$0.6m$
Width, w_b	$0.05m$
Thickness, h_b	$0.003m$
Young's Modulus, E_b	$65 \times 10^9 N/m^2$
Density, ρ	$2650kg/m^2$

Table B.1: Parameters of the simply supported beam.

Appendix C

Shim Parameters

Width, w_{sh}	$0.05m$
Thickness, h_{sh}	$0.00034m$
Young's Modulus, E_{sh}	$65 \times 10^9 N/m^2$
Density, ρ_{sh}	$2650 kg/m^2$
Length, L_{sh}	$0.005m$

Table C.1: Parameters of the shim material.

Appendix D

PIC151 PZT Piezoelectric Parameters

Charge Constant, d_{31}	$-210 \times 10^{-12} m/V$
Voltage Constant, g_{31}	$-11.5 \times 10^{-3} Vm/N$
Coupling Coefficient, k_{31}	0.340
Capacitance, C_p	$0.105 \mu F$
Width, w_s w_a	$0.025m$
Thickness, h_s h_a	$0.25 \times 10^{-3} m$
Length, l_s l_a	$0.0699m$
Young's Modulus, E_s E_a	$63 \times 10^9 N/m^2$

Table D.1: Parameters of the PIC151 piezoelectric patches.

Bibliography

[1] G. S. Agnes. Active/passive piezoelectric vibration suppression. *In: Proceedings of SPIE: Smart Structures and Materials 1994: Passive Damping*, 2193:24–34, 1994.

[2] S. Behrens and A. J. Fleming. Negative capacitor for multiple mode shunt damping of a piezoelectric laminate beam. Technical Report EE0045, Electrical and Computer Engineering, University of Newcastle, October 2000.

[3] P. Bisegna, G. Caruso, D. Del Vescovo, S. Galeani and L. Menini. Semi-active control of a thin piezoactuated structure. *In: Proceedings of SPIE: Smart Structures and Materials 2000: Damping and Isolation*, 3989:300–311, 2000.

[4] W. W. Clark. Semi-active vibration control with piezoelectric materials as variable-stiffness actuators. *In: Proceedings of SPIE: Smart Structures and Materials 1999: Passive Damping and Isolation*, 3672:123–130, 1999.

[5] B. Clephas. *Adaptronics and Smart Structures - Basics, Material, Design, and Applications*, Chapter 6.2, page 106. Springer, 1999.

[6] C. L. Davis and G. A. Lesieutre. An actively-tuned soild state piezoelectric vibration absorber. *In: Proceedings of SPIE: Smart Structures and Materials 1998: Passive Damping and Isolation*, 3327:169–182, 1998.

[7] C. L. Davis and G. A. Lesieutre. An actively tuned solid-state vibration absorber using capacitance shunting of piezoelectric stiffness. *J. of Sound and Vibration*, 232(3):601–617, 2000.

[8] J. J. Dosch, D. J. Inman and E. Garcia. A self-sensing piezoelectric actuator for collocated controller. *J. of Intelligent Material Systems and Structures*, 3:166–185, January 1992.

[9] D. L. Edberg, A. S. Bicos, C. M. Fuller, J. J. Tracy, and J. S. Fechter. Theoretical and experimental studies of a truss incorporating active members. *J. of Intelligent Materials Systems and Structures*, 3:333, 1992.

[10] C. R. Fuller, S. J. Elliott and P. A. Nelson. *Active Control of Vibration.* Academic Press, 1996.

[11] N. W. Hagood, W. H. Chung and A. von Flowtow. Modeling of piezoelectric actuator dynamics for active structural control. *J. of Intelligent Material Systems and Structures*, 1:327–353, July 1990.

[12] N. W. Hagood and E. F. Crawley. Experimental investigations of passive enhancement of damping space structures. *J. of Guidance, Control and Dynamics*, 14(6):1100, 1991.

[13] N. W. Hagood and A. von Flotow. Damping of structure vibrations with piezoelectric materials and passive electrical networks. *J. of Sound and Vibration*, 14(2):243, 1991.

[14] J. J. Hollkamp. Multimode passive vibration suppression with piezoelectric materials and resonant shunts. *J. of Intelligent Materials Systems and Structures*, 5:4, 1994.

[15] R. C. Juvinall and K. M. Marshek. *Fundamentals of Components Design.* John Wiley and Sons, 2nd edition, 1991.

[16] L. Meirovitch. *Elements of Vibration Analysis.* McGraw-Hill, Sydney, 2nd edition, 1996.

[17] S. O. R. Moheimani. Experimental verification of the corrected transfer function of a piezoelectric laminate beam. *IEEE Transactions on Control Systems Technology*, 8(4):660–666, July 2000.

[18] H. R. Pota, S. O. R. Moheimani and M. Smith. Resonant controllers for smart structures. *In: IEEE Conference on Decision and Control, December 1999 Phoenix, Arizona, USA*, pages 631–636, 1999.

[19] S. S. Rao. *Mechanical Vibrations.* Addison-Wesley Publishing Company, 3rd edition, 1995.

[20] C. Richard, D. Guyomar, D. Audigier and H. Bassaler. Enhance semi-passive damping using continuous switching of a piezoelectric devices on an inductor. *In: Proceedings*

of SPIE: Smart Structures and Materials 2000: Damping and Isolation, 3989:288–299, 2000.

[21] C. Richard, D. Guyomar, D. Audigier and G. Ching. Semi-passive damping using continuous switching of a piezoelectric device. *In: Proceedings of SPIE: Smart Structures and Materials 1994: Passive Damping and Isolation*, 3672:104–111, 1999.

[22] R. H. S. Riodan. Simulated inductors using differential amplifiers. *IEE Electronic Letters*, 3(2):50–51, 1967.

[23] M. S. Tsai and K. W. Wang. Some insights on active-passive hybrid piezoelectric networks for structural controls. *In: Proceedings of SPIE: Smart Structures and Materials 1997: Passive Damping and Isolation*, 3045:82–93, 1997.

[24] M. S. Tsai and K. W. Wang. On the structural damping characteristics of active piezoelectric actuators with passive shunt. *J. of Sound and Vibration*, 221(1):1–22, 1999.

[25] K. W. Wang. Structural vibration suppression via parametric control actions - piezoelectric materials with real-time semi-active networks. *Series on Stability, Vibration and Control of Structures*, 1:112–134, 1995.

[26] C. C. Won. Piezoelectric transformer. *J. of Guidancce, Control, and Dynamics*, 18:96–101, 1995.

[27] S. Y. Wu. Piezoelectric shunts with parallel R-L circuit for smart structural damping and vibration control. *In: Proceedings of SPIE: Smart Structures and Materials 1996: Passive Damping and Isolation*, 2720:259–269, March 1996.

[28] S. Y. Wu. Method for multiple mode shunt damping of structural vibration using a single PZT transducer. *In: Proceedings of SPIE: Smart Structure and Materials 1993: Smart Structures and Intelligent System*, 3327:159–168, March 1998.

[29] S. Y. Wu. Multiple PZT transducer implemented with multiple-mode piezoelectric shunt for passive vibration damping. *In: Proceedings of SPIE: Smart Structures and Materials 1999: Passive Damping and Isolation*, 3672:112–122, March 1999.

[30] S. Y. Wu and A. S. Bicos. Structure vibration damping experiments using improved piezoelectric shunts. *In: Proceedings of SPIE: Smart Structures and Materials 1997: Passive Damping and Isolation*, 3045:40–50, March 1997.